Evidence of the complexity of aerosol transport in the lower troposphere on the Namibian coast during AEROCLO-sA

Patrick Chazette[1], Cyrille Flamant[2], Julien Totems[1], Marco Gaetani[2,3], Gwendoline Smith[1,3], Alexandre Baron[1], Xavier Landsheere[3], Karine Desboeufs[3], Jean-François Doussin[3], and Paola Formenti[3]

[1]Laboratoire des Sciences du Climat et de l'Environnement (LSCE), Laboratoire mixte CEA-CNRS-UVSQ, UMR CNRS 1572, CEA Saclay, 91191 Gif-sur-Yvette, France
[2]LATMOS/IPSL, Sorbonne Université, CNRS, UVSQ, Paris, France
[3] Laboratoire Interuniversitaire des Systèmes Atmosphériques (LISA) UMR CNRS 7583, Université Paris-Est-Créteil, Université de Paris, Institut Pierre Simon Laplace, Créteil, France.

Correspondence to: Patrick Chazette (patrick.chazette@lsce.ipsl.fr)

Abstract. The evolution of the vertical distribution and optical properties of aerosols in the free troposphere, above stratocumulus, is characterized for the first time over the Namibian coast, a region where uncertainties on aerosol-cloud coupling in climate simulations are significant. We show the high variability of atmospheric aerosol composition in the lower and middle troposphere during the AEROCLO-sA field campaign (22 August - 12 September 2017) around the Henties Bay supersite, using a combination of ground-based, airborne and space-borne lidar measurements. Three distinct periods of 4 to 7 days are observed, associated with increasing aerosol loads (aerosol optical thickness at 550 nm ranging from ~ 0.2 to ~0.7), as well as increasing lofted aerosol layer depth and top altitude. Aerosols are observed up to 6 km above mean sea level during the later period. Aerosols transported within the free troposphere are mainly polluted dust (predominantly dust mixed with smoke from fires) for the first 2 periods (22 August-1 September 2017) and smoke for the last part (3-9 September) of the field campaign. As shown by lagrangian back trajectory analyses, the main contribution to the aerosol optical thickness over Henties Bay is shown to be due to biomass burning over Angola. Nevertheless, in early September, the highest aerosol layers (between 5 and 6 km above mean sea level) seem to come from South America (southern Brazil, Argentina and Uruguay) and to reach Henties Bay after 3 to 6 days. Aerosols appear to be transported eastward by the mid latitude westerlies and towards Southern Africa by the equatorward moving cut-off low originating from within the westerlies. All the observations show a very complex mixture of aerosols over the coastal regions of Namibia that must be taken into account when investigating aerosols radiative effects above stratocumulus clouds in the south east Atlantic Ocean.

Keywords: dust, biomass burning aerosols, regional transport, atmospheric dynamics, back trajectories, lidar

1   Introduction

The western coast of southern Africa is a complex area in terms of both atmospheric composition, circulation, and climate, with aerosol-radiation-cloud interactions playing a significant role. A large part of this complexity is related to atmospheric circulation associated with a low-laying coastal strip next to an elevated continental plateau covering most of the sub-continent, as well as fast-evolving meteorological synoptic patterns largely controlled by

the St Helena anticyclone over the Atlantic and the mid-latitude westerlies on the poleward edge of this high-pressure system (Tyson and Preston-White, 2000).

The region is characterized by a complex aerosol composition linked to the variety of the sources. Biomass burning aerosols (BBA) regions over equatorial Africa (from both man-set fires and wild-fires) contribute to the regional and seasonal haze with the highest recorded aerosol optical thickness (Swap et al., 2003). Natural aerosols include i) mineral dust from point sources along the Namibian coast lines, as well as in the Etosha Pan in Namibia and in the Makgadikgadi Pan in Botswana (Ginoux et al., 2012; Vickery et al., 2013), and ii) marine sea spray and biogenic aerosols due to the strong productivity of the northern Benguela Upwelling System of the coast of Namibia (Andreae et al., 2004; Bates et al., 2001). Additional regional anthropogenic pollution is related to industrial emissions from South Africa and port activities in Namibia, together with ship emissions along the Namibian coast (Johansson et al., 2017).

The atmosphere over the coastal region of southern Africa is also characterized by a quasi-permanent stratocumulus deck, topping the marine boundary layer, and by a considerable thermodynamical stratification (Keil and Haywood, 2003), that limits the aerosol vertical mixing and exchange. Nevertheless, various authors (e.g. Diamond et al., 2018; Formenti et al., 2018; Zuidema et al., 2018) have provided evidence that BBA and dust aerosols emitted over the elevated continental plateau and transported in layers above the stratocumulus deck might penetrate and mix in the marine boundary layer (MBL). Others have also shown that the stratification of the aerosol layers over the south east Atlantic evolves with the distance from the coastline, increasing their ability to penetrate the stratocumulus deck (e.g. Adebiyi and Zuidema, 2016; Gordon et al., 2018).

Marine stratocumulus are particularly sensitive to aerosol perturbations due to relatively low background aerosol concentrations (Oreopoulos and Platnick, 2008). As a matter of fact, the vertical distribution of aerosols (and absorbing aerosols in particular) as well as their location with respect to bright low-level clouds (above or below) is of paramount importance as it significantly influences the indirect radiative effect (e.g. Ramanathan et al., 2007), the vertical profile of radiative heating in the atmosphere (e.g. Léon et al., 2002; Ramanathan et al., 2007; Raut and Chazette, 2008) and, in turn, the stability of the atmosphere, thereby modifying convective and turbulent motions and clouds (e.g. Ackerman et al., 2000; McFarquhar and Wang, 2006).

In this context, the coastal southern Africa region is arguably one of the regions where the aerosol-radiation-cloud interactions are strongest in the world (Adebiyi et al., 2015; Fuchs et al., 2017). However, state-of-the-art climate models diverge by several W m^{-2} when attempting to calculate the regional direct radiative effect over coastal Southern Africa (Myhre et al., 2013; Stier et al., 2013) ranging from negative (-3 W m^{-2}) to strong positive forcing (+5 Wm^{-2}) for mean seasonal averages. These model shortcomings, that can also affect the simulation of climate features in distant areas (e.g., rainfall anomalies in Brazil, the position of the Intertropical Convergence Zone; Jones et al., 2009; Jones and Haywood, 2012), are mainly due to a limited knowledge of aerosol properties, and of the vertical position of aerosol and cloud layers.

The main purpose of this article is to characterise the temporal and spatial evolutions of the vertical distribution of aerosol optical properties observed along the coastline of Namibia, in Henties Bay, in August and September 2017 during the Aerosols, Radiation and Clouds in southern Africa (AEROCLO-sA) field campaign (Formenti et al., 2019). The evolution of the vertical distribution of aerosols properties is examined as a function of the synoptic conditions and aerosol source emissions. The investigation is conducted by analysing a combination of ground-

76   based, airborne and space-borne lidar measurements, together with back-trajectory and numerical weather forecast

77   model analyses, as well as complementary space-borne passive sensors observations.

78   Section 2 presents the observations and provides a description of the ground-based, airborne and space-borne

79   active and passive remote sensing instruments used during the field campaign, together with complementary

80   numerical simulation tools. Section 3 presents the evolution of the vertical profiles of aerosols during the

81   campaign, together with the main optical and geometrical characteristics of the lofted aerosol layers and identifies

82   three distinct periods with increasing aerosol load. The variability of the vertical distribution of aerosols around

83   Henties Bay during the later period is assessed using lidar and dropsonde measurements acquired over the ocean,

84   as detailed in Section 4. In Section 5, we investigate the different origins and transport pathways of aerosols in the

85   free troposphere towards Henties Bay during the three periods. The last section is dedicated to the summary and

86   conclusion. The description of the ground-based lidar is given in Appendix A, together with the calibration and

87   data inversion processes.

88   **2   Observations and simulations**

89   The AEROCLO-sA supersite of Henties Bay (-22° 6' S, 14° 17' E, Figure 1) belongs to the Sam Nujoma Marine

90   and Coastal Resources Research Centre (SANUMARC) of the University of Namibia in the Orongo region. It has

91   been selected because of its geographical position: bounded by the Atlantic Ocean on its western side and by the

92   Namib desert, ~800 m above the mean sea level (AMSL), on its eastern side (Formenti et al., 2019). The analysis

93   presented here relies mainly on active and passive remote sensing observations acquired from i) ground-based

94   instruments deployed in Henties Bay, namely an Aerosol Lidar System (ALS) 450® (Leosphere Inc, Saclay,

95   France) operating at a wavelength of 355 nm and a sun photometer from the National Aeronautics and Space

96   Administration Aerosol Robotic Network (AERONET), ii) the airborne lidar LEANDRE (Lidar Embarqué pour

97   l'Etude des Aérosols, Nuages, Dynamique, Rayonnement et Espèces minoritaires) nouvelle Génération (LNG),

98   working in the Rayleigh-Mie scattering mode, installed on the Service des Avions Français Instrumentés pour la

99   Recherche en Environnement (SAFIRE) Falcon 20 and iii) space-borne instruments, namely the Cloud-Aerosol

100   Lidar with Orthogonal Polarization (CALIOP), the Cloud-Aerosol Transport System (CATS) lidar and the

101   Moderate-Resolution Imaging Spectroradiometer (MODIS). The available measurements are summarized in Table

102   1 against the date and the universal time count (UTC). The synergy between ground-based lidar measurements,

103   space-borne observations (aerosol typing and aerosol optical thickness (AOT)) and those of the sun photometer

104   (AOT and Ångström exponent) is used to better constrain the retrieval of the aerosol optical parameters (see

105   Appendix A): aerosol extinction coefficient (AEC), lidar ratio (LR) and particle depolarisation ratio (PDR). The

106   space-borne lidar-derived aerosol types are associated with prescribed LRs (see Section 2.4) that are used for the

107   inversion of the ground-based lidar.

108   **Table 1: Data available during the field campaign on August and September 2017 from: the ground-based ALS lidar**
109   **and AERONET sun photometer in Henties Bay, the airborne LNG lidar, dropsonde released from the Falcon 20, as**
110   **well as the CATS and CALIOP space-borne lidars. The line highlighted in bold indicates when the AERONET inversion**
111   **allows the retrieval of a relevant value for the lidar ratio (level 2 data). The aerosol typing as provided by CALIOP and**
112   **CATS is also indicated for overpasses in the vicinity of Henties Bay.**

Date	ALS measurement	F20 flight LNG & dropsonde	**Coupling ALS/**	**CALIOP** Orbit close to the site	**CATS**

	time (UTC)	measurement time (UTC)	**AERONET**		**Overpass time (UTC)**
22 Aug	1400-2300	-	Yes	-	-
23 Aug	1645-2330	-	Yes	-	0342-0357 Smoke
27 Aug	1545-1700	-	Yes	-	-
28 Aug	1030-1230	-	Yes	10.2017-08-28T00-08-17ZN 10.2017-08-28T12-26-48ZD Polluted dust/Smoke	-
29 Aug	1730-2250	-	No	10.2017-08-29T23-55-43ZN Smoke	0122-0207 Smoke
30 Aug	1800-2000	-	No		0047-0102 Smoke
31 Aug	1430-2100	-	Yes	10.2017-08-31T12-57-28ZD Smoke/Polluted dust	1452-1507 Smoke/Dust
02 Sep	0930-1130 1715-1900	-	Yes	10.2017-09-02T12-44-54ZD Smoke/Polluted dust	-
03 Sep	**1400-1540**	-	Yes	-	-
04 Sep	2330-2400	-	No	10.2017-09-04T00-13-44ZN Smoke	-
05 Sep	1400-1500	Flight 6 LNG: ~1000 Dropsonde #5: 0952	No	-	2204-2219 Smoke
06 Sep	0830-1030	Flight 8	Yes	-	1258-1313

		LNG: ~0830 and ~0900 Dropsondes #3 and #4: 0843 and 0908			Smoke/dust
07 Sep	1600-1900	-	No	-	2156-2211 Smoke
08 Sep	1300-1500	-	No	-	2052-2107 Smoke
09 Sep	0900-1200	-	Yes	-	2001-2016 Smoke
11 Sep	1040-1140	-	Yes	-	-

113
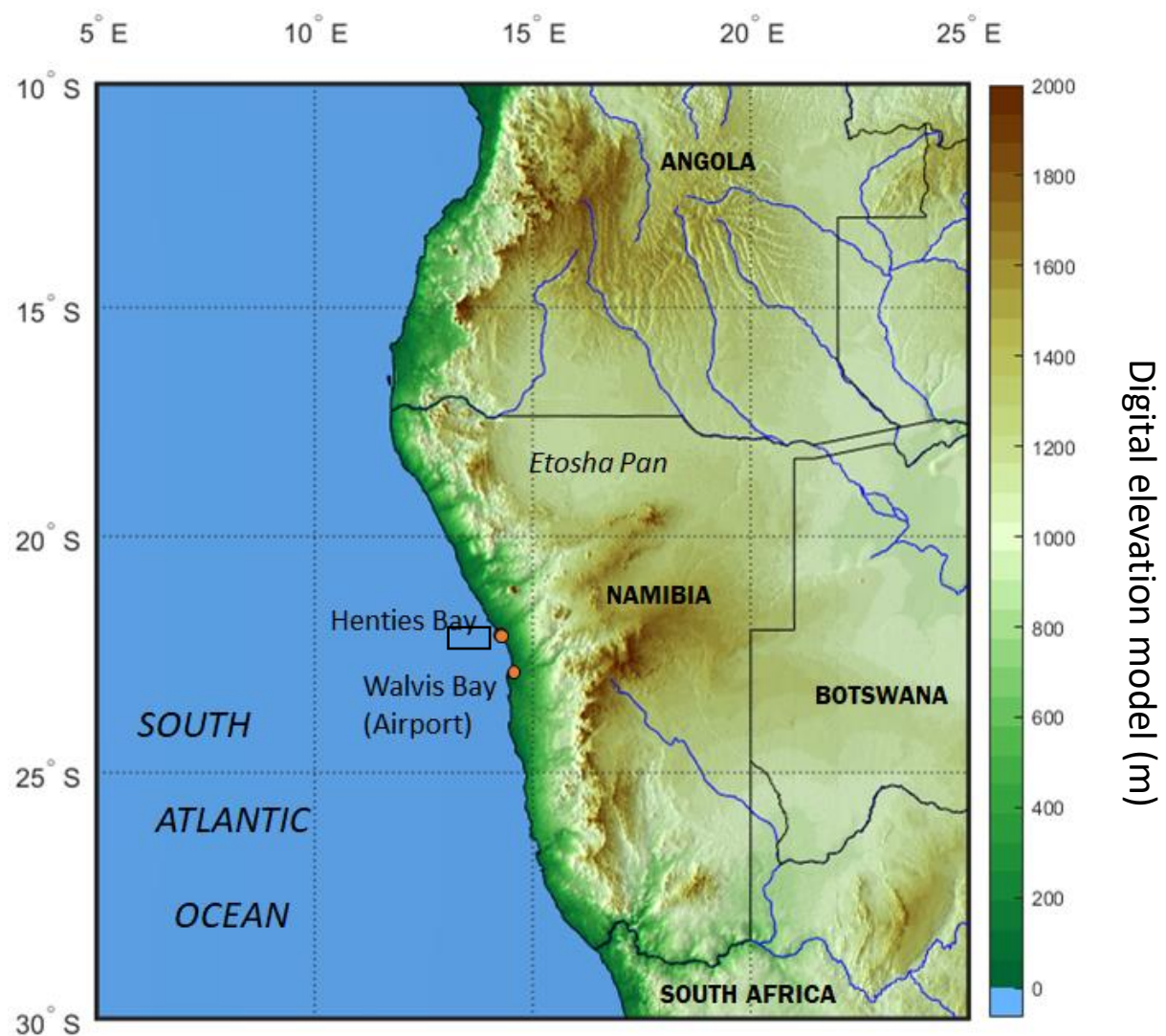
114

2.1   Ground-based lidar

The ALS lidar measurements were carried out continuously between 22 August and 13 September, 2017. The data coverage for aerosol study is low because of the quasi-ubiquitous presence of marine stratocumulus and fog during a large part of the observation days. The fog opacity was often such that the laser beam was fully attenuated after a few hundred meters. We therefore considered average profiles taken during periods when no low-level clouds or fog events are observed, i.e. between about 1 and 4 hours on a given day (see Table 1). The description of the lidar is given in Appendix A, together with the calibration and data inversion processing.

2.2   AERONET sun photometer

The site of Henties Bay was equipped with a sun and sky scanning spectral radiometer manufactured by CIMEL Inc (Paris, France) and belonging to the AERONET automatic and global network of sun photometers providing long-term and continuous monitoring of aerosol optical, microphysical and radiative properties (http://aeronet.gsfc.nasa.gov/). Eight spectral bands are generally used between 340 and 1020 nm. The aerosol optical thickness at the lidar wavelength of 355 nm (AOT_{355}) is assessed using the Ångström exponent (Ångström, 1964) and the sun photometer AOT at 380 and 440 nm (e.g. Hamonou et al., 1999). We use level 2.0 (cloud screened and quality-assured) aerosol optical thickness (AOT) data in the following. The total uncertainty on AOT is $<\pm0.01$ for $\lambda>440$ nm and $<\pm0.02$ for $\lambda<440$ nm (Holben et al., 1998). Nevertheless, additional bias may exist when thin clouds are present and not screened in the AERONET level-2 products (Chew et al., 2011). To limit this, ground-based lidar profiles are used to identify the presence of clouds when sun photometer observations are available.

2.3   Airborne measurements

In this study, we also analyse extinction coefficients over the Atlantic, and in the vicinity of Henties Bay, acquired with the LNG Lidar (Bruneau et al., 2015) flown on the SAFIRE Falcon 20 on 5 and 6 September. We only use the 532 nm channel because the high level of noise in the high spectral resolution 355 nm channel. Hence, the lidar was operated as a simple backscatter Rayleigh-Mie lidar. The Falcon 20 operated from Walvis Bay, on the western coast of Namibia, roughly 100 km south of Henties Bay where the AEROCLO-sA supersite was located. Details on the Falcon payload as well as the on the flight plans conducted during these two days can be found in Formenti et al. (2019). In addition to the LNG data, we also make use of dynamical and thermodynamical data acquired offshore of Namibia with the Vaisala dropsonde system.

During the first flight (flight #6 in the morning of 5 September 2017), the Falcon operated from 0736 to 1014 UTC. It flew mostly above the continent to monitor dust emissions over the Etosha pan (see Formenti et al., 2019). The later portion of the flight was conducted over the sea (from 0930 to 1014 UTC), and a dropsonde was launched from 13.78°E/ 21.69°S at 0952 UTC. For the second flight (flight #9 in the morning of 6 September 2017), the Falcon 20 operated from 0703 to 0927 UTC and flew over the ocean from 0820 to 0927 UTC. Two dropsondes were launched from 11.92°E / 19.87°S at 0843 UTC and from 13.41°E / 22.23°S at 0908 UTC.

153 The LNG data over the sea are inverted using the same procedure as for the ground-based ALS lidar (see Appendix

154 A) and utilizing the same LR vertical distribution (see values retrieved in Henties Bay for the two days in Section

155 3).

156 **2.4 Spaceborne observations**

157 **2.4.1 CALIOP & CATS**

158 The Cloud-Aerosol LIdar with Orthogonal Polarization (CALIOP) has been flying onboard the Cloud-Aerosol

159 Lidar Pathfinder Satellite Observation (CALIPSO) since 2006 (https://www-calipso.larc.nasa.gov/products/).

160 Details on the CALIOP instrument, data acquisition, and science products are given by Winker et al. (2007). In

161 this work, we use CALIOP level-2 data, version 4.10 (Kim et al., 2018), which was corrected for aerosol typing,

162 as noted in Burton et al. (2012). The aerosol types identified in the free troposphere (FT) are typically polluted

163 dust and elevated smoke (see example in Appendix A).

164 The CATS lidar orbited between 375 and 435 km onboard the non-sun-synchronous International Space Station

165 (Yorks et al., 2016). It operated between January 2015 and October 2017 with the objective of measuring some

166 cloud and aerosols properties which are useful for climate study. CATS flew over Namibia at various times during

167 the AEROCLO-sA field campaign (Table 1). We mainly used the aerosol typing derived from CATS

168 measurements, which is similar to the one established for CALIOP. The correspondence between the aerosol

169 typing derived from CALIOP and CATS measurements are given in the Table 2. It should be noted that not all the

170 aerosol types are named exactly in the same way. An example of aerosol typing is given in Appendix A.

171

172 **Table 2: Lidar ratio (LR) corresponding with the CATS- and CALIOP-derived aerosol typing.**

CALIOP/CATS Aerosol typing	Lidar ratio (sr) at 532 nm
Polluted continental or smoke/Polluted continental	70/65
Clean continental/Clean-background	53/55
Clean marine/Marine	23/25
Dust/Dust	44/45
Polluted dust/Dust mixture	55/35
Elevated smoke/Smoke	70/70
Dusty marine/Marine mixture	37/45

173

174 **2.4.2 MODIS**

175 The MODIS instruments (King et al., 1992; Salmonson et al., 1989) are aboard the Aqua and Terra platforms

176 (http://modis-atmos.gsfc.nasa.gov). The polar orbit of Terra (http://terra.nasa.gov) passes over the equator from

177 north to south in the morning, whereas Aqua (http://aqua.nasa.gov) has its ascending node over the equator during

178 the afternoon. They provide a complete coverage of the Earth surface in one to two days with a resolution between

179 250 and 1000 m at ground level depending on the spectral band. We use the Terra and Aqua AOT at 550 nm from

180 the MODIS aerosol product level-2 data. Both products are given with a spatial resolution of 10×10 km^2 at nadir.

181 The uncertainty in the AOT retrieval (Remer et al., 2005) over land (ocean) is 0.15±0.05AOT (0.05±0.03AOT).
182 We will only use data over the sea because Henties Bay is a coastal site affected by the sea breeze and bordered
183 by a strong topography (Figure 1). This is associated with the lowest levels of uncertainty. The thermal anomalies
184 derived from the MODIS fire product (e.g. Ichoku et al., 2008) are also used
185 (https://modis.gsfc.nasa.gov/data/dataprod/mod14.php).

186 2.5 Modelling

187 The meteorological patterns are studied using Meteorological fields provided by the 6-hourly operational analyses
188 of the European Centre for Medium-Range Weather Forecasts (ECMWF, http://apps.ecmwf.int/datasets/, Dee et
189 al. (2011)). We also use the near real time analyses of atmospheric dynamics and aerosols from the Copernicus
190 Atmosphere Monitoring Service (CAMS, https://atmosphere.copernicus.eu/). The calculations for synoptic
191 analysis are computed on a 0.75-degree horizontal regular grid. Daily means are computed by averaging time steps
192 at 03:00, 09:00, 15:00 and 21:00 UTC of daily forecasts initialised at 00.00 UTC. For local analyses, the
193 meteorological wind fields are computed by using 1-h data on a 0.25-degree horizontal regular grid from the Fifth
194 ECMWF Reanalysis (ERA5, https://www.ecmwf.int/en/forecasts/datasets/archive-datasets/reanalysis-
195 datasets/ERA5, Hoffmann et al., 2018). The back trajectories analyses are based on the Hybrid Single Particle
196 Lagrangian Integrated Trajectory (HYSPLIT) model (Draxler and Rolph, 2014; Stein et al., 2015). The wind fields
197 used as input from the HYSPLIT model are from GDAS (Global Data Assimilation System,
198 http://www.ncep.noaa.gov/) at 0.5° horizontal resolution. The isentropic ensemble mode with 24 individual back
199 trajectories is used to take into account the transport trajectory spread associated with the wind field variability
200 around the trajectories starting point. Using different modelling approaches also allows the consistency of results
201 to be verified.

202 3 Temporal evolution of the aerosol properties and vertical distribution over Henties Bay

203 3.1 Identification of periods from the total AOT

204 The temporal evolution of the AOT at 550 nm derived from passive remote sensing observations (MODIS and the
205 Henties Bay sun photometer) and 6-hourly CAMS fields between 22 August and 9 September 2017 are shown in
206 Figure 2a. For CAMS, both the AOT extracted from the grid cell centred on Henties Bay and the average AOT
207 calculated on a 3x3 grid-point box surrounding the site are shown. There are little differences between the two
208 CAMS-derived AOTs, which highlight the homogeneity of aerosol plumes overpassing Henties Bay according to
209 the model and during that period. The MODIS AOT at 550 nm plotted in Figure 2a is a daily synthesis of Terra
210 and Aqua products extracted over the sea only (see the black rectangle in Figure 1), to avoid mixing the effects of
211 coast, topography and surface albedo in the AOT retrievals. Overall, the AOTs from CAMS match within 0.1 the
212 ones derived from both MODIS and the sun photometer, except on 2 September and 7-8 September. These
213 discrepancies on AOT may be also explained by the coarse spatio-temporal sampling of the model, which is
214 insufficient to highlight the sharp variation in AOT due to a very localized aerosol features during these 3 days.
215 As a result, even small differences in the simulation of the weather conditions could lead to substantial differences
216 in AOT for specific locations, especially when AOT values are rather low. Note that no significant precipitation
217 event was recorded during the field campaign, so that we can exclude any CAMS misrepresentation of wet

218 deposition processes around Henties Bay. In addition, CAMS simulations show that the AOT is essentially due to
219 organic matter (i.e. biomass burning aerosols), the contribution from non-biomass aerosol can then be excluded as
220 well. On 2 September a minimum in AOT is observed by the sun photometer which is not reproduced by CAMS
221 simulations (even though a local minimum in the CAMS AOT can be seen). During this day, the mid-tropospheric
222 circulation was characterised by a low-pressure system located offshore of Henties Bay, juxtaposed to a high-
223 pressure system over South Africa, resulting in a small river of smoke descending along the coast that CAMS is
224 simulating too far east over Henties Bay. On 7-8 September, the sun photometer- and MODIS-derived AOTs are
225 larger than the one computed from CAMS. This could be related to the presence of unscreened optically thin clouds
226 such as the ones observed in the ground-based lidar data on 8 September (Figure A2d) and/or to the heterogeneity
227 of the meteorological field. Indeed, on 7-8 September, an elongated high pressure dominating over the continent,
228 led to the channelling of the smoke from the north-west that is slightly mis-located in the CAMS analyses.
229 In Figure 2a, three distinct periods can be identified based on the temporal evolution of both the remote sensing
230 instruments and the CAMS-derived AOT. The optical and geometrical properties of the aerosol layers derived
231 from the remote sensing instruments over Henties Bay during the 3 periods are summarized in Table 3. The first
232 period P_1 (22-28 August 2017, see Figure 2a) is characterized by an averaged AOT of ~0.20 at 550 nm, while for
233 the second period P_2 (28 August – 1 September 2017, see Figure 2a) the AOT increases to ~0.4. During the third
234 period P_3 (3-11 September 2017), the average AOT is higher than during P_2 and around 0.55 at 550 nm (see Figure
235 2). 2 September can be considered as a transition period between P_2 and P_3. The variability of the CAMS-derived
236 AOT is much larger during P_3 than during P_1 and P_2 which may show greater variability in atmospheric transport
237 conditions. The sunphotometer derived Angstrom exponent (AE) evolves during the period of interest, with AE~1
238 during P_1 et AE~1.4 during P_2 and P_3 (see Table 3), suggesting the presence of larger aerosol in the atmospheric
239 column during P_1.

240 **3.2   Aerosol vertical profiles**

241 The AEC profiles shown in Figures 3 to 7 are obtained in cloud free conditions using a standard inversion
242 procedure detailed in Appendix A. Most AEC profiles show clear air with low particle concentrations between the
243 planetary boundary layer (PBL) and the elevated aerosol layer, with the notable exception of 2 September in the
244 afternoon, when aerosols are mainly observed in the PBL (Figure 5b). Figure 2b shows the AOTs at 355 nm
245 calculated from the lidar-derived AEC profiles between the surface and ~6.5 km AMSL, as well as partial column
246 AOTs in the FT for three different altitude ranges where aerosol loads can be highlighted: namely [1500-3000[,
247 [3000-5000[and [5000 6000[m (green, grey and red bars in Figure 2b, respectively). The temporal evolution of
248 the partial column AOTs corroborate the existence of the 3 periods. During P_3, we observe AOTs in excess of 0.1
249 between 5000 and 6000 m AMSL for at least 4 days (3, 6, 7 and 11 September) whereas partial AOTs in that
250 height range are negligible in the previous two periods. AOT values as high as 0.4 are observed on 6 September.
251 The increase in the lidar-derived column AOT (blue bars in Figure 2b) during P_3 is also well correlated to the
252 increase of the partial column AOT in the 1500-3000 m AMSL.
253 We note a significant increase in terms of the lidar-derived thickness of elevated aerosol layer between the 3
254 periods (~1-2.5 km during P_1, ~2.5-3 km during P_2 and ~2.5-5 km during P_3, Table 3) as well as in terms of
255 maximum AEC in the FT (~0.1 km^{-1} during P_1, ~0.25 km^{-1} during P_2 and ~0.3 km^{-1} during P_3, Table 3) as seen in
256 the AEC profiles (compare Figure 3 for P_1 with **Erreur ! Source du renvoi introuvable.** for P_2). The height of

257 the base of the elevated aerosol layer also increases between P_1 and P_2, from ~1-1.5 km AMSL to more than 2 km

258 AMSL (Table 3), but appears more variable during P3 (from ~1 to 3 km AMSL, Figure 6 and Figure 7). These

259 changes in optical and geometrical properties of the aerosols in the FT are related to the variability of long-range

260 transport over the area, as discussed in Section 5.

261 CALIPSO and CATS retrievals suggest differences in the FT aerosols between P_1/P_2 and P_3, with more occurrence

262 of polluted dust (55 sr) in P_1/P_2 and polluted continental or smoke (70 sr) in P_3. In the PBL, during P_1/P_2, the

263 retrieved low value of LR (i.e. 23 sr) required to reproduce the sunphotometer AOT is consistent with the presence

264 of clean marine aerosols in the PBL (e.g. Flamant et al., 1998). The retrieved higher LRs required in P_3 indicate

265 the presence of other aerosol types, which may include smoke (i.e.70 sr) or a mixture of smoke and terrigenous

266 aerosols (i.e. 55 sr). The latter LR value suggests the presence of terrigenous aerosols mixed with smoke,

267 corresponding to the aerosol typing "Polluted Dust". During P_3, aerosols in the FT are mainly identified as "smoke"

268 (based on the CALIOP and CATS typing). Very few sun photometer data are available for LR retrieval due to the

269 quasi permanent presence of a cloud cover over Henties Bay during the cycles of almucantar measurements.

270 Nevertheless, such a measurement could be obtained during P_3, on 3 September 2017 at ~14:10 UTC. A sun

271 photometer-derived LR of ~63 sr at 532 nm has been computed from the backscatter phase function and the single

272 scattering albedo (Dubovik et al., 2000). It was found to match the LR associated with the smoke type of CALIOP

273 and CATS (i.e. 65-70 sr at 532 nm).

274 The PDR is computed for each AEC profile given in Figures 3 to 7. The PBL is associated with the lower PDR

275 (i.e. < 2-3%), mainly during P_1 and P_2. This argues for the presence of hydrophilic spherical particles as marine

276 aerosols. Within the free troposphere the PDR is higher, mainly between 5 and 10% and may correspond to a

277 mixing of biomass burning and dust aerosols as often observed in biomass burning aerosol plume over others areas

278 (e.g. Chazette et al., 2015; Kim et al., 2009). This is consistent with the hypothesis of dust mobilization and mixing

279 by convection in biomass burning regions. Above the PBL larger PDR can be observed and may indicate a higher

280 relative presence of dust. This should be taken with caution as AEC values are low for these layers and uncertainties

281 are therefore higher.

282

283 **Table 3. Properties of aerosol layers above the Henties Bay site as derived from the ground-based lidar, CALIOP,**
284 **CATS, the sun photometer and MODIS: lidar ratios for the free troposphere (LR$_{FT}$) and the planetary boundary layer**
285 **LR$_{PBL}$ at 532 nm, ground-based lidar (GBL)-derived AOT$_{GBL}$ at 355 nm and its uncertainty (detection noise and**
286 **atmospheric variability), sunphotometer-derived AOT$_{phot}$ at 355 nm and 550 nm, sunphotometer-derived Ångström**
287 **exponent (AE), MODIS-derived AOT$_{MODIS}$ in 0.5°x0.5° area over the sea close to Henties Bay, free troposphere aerosol**
288 **layer (FTA) thickness and bottom height and maximum of the aerosol extinction coefficient (AEC$_{max}$) in the UAL. P$_1$**
289 **and P$_2$ correspond to periods when the AFT is mostly composed of "polluted dust", and P$_3$ corresponds to period when**
290 **smoke aerosols dominate the composition of the UAL.**

Date UTC	LR_{FT} LR_{PBL} (sr)	AOT$_{GBL}$ at 355 nm	AOT$_{phot}$ at 355 nm *at 550 nm*	AE	AOT$_{MODIS}$ 550 nm 0. 5°x0. 5°	FTA width (km)	FTA bottom height (km)	AEC$_{max}$ in the FTA (km^{-1})
Period P$_1$								
22/08 1400-2300	**55** 23	0.36±0.02	0.37±0.02 *0.22±0.01*	1.15±0.15	0.26±0.03	~1	~1.5	~0.15

23/08 1645-2330	**55** 23	0.31±0.03	0.34±0.01 *0.22±0.01*	0.95±0.05	0.23±0.03	~1.5	~1	~0.1
27/08 1545-1700	**55** 23	0.32±0.01	0.33 *0.18*	1.27	Clouds	~2.5	~1.5	~0.1
Period P₂								
28/08 1030-1230	**55** 23	0.63±0.03	0.59±0.04 *0.24±0.04*	1.5±0.05	0.25±0.12	~3	~2	~0.2
29/08 1730-2250	**55** 23	0.60±0.02	-	-	Clouds	~2	~3	~0.2
30/08 1800-2000	**55** 23	0.82±0.04	-	-	0.30±0.05	~2.5	~2.3	~0.3
31/08 1430-2100	**55** 23	0.83±0.01	0.85±0.02 *0.42±0.08*	1.4±0.04	0.44±0.05	~2.5	~2.5	~0.3
Transition period								
02/09 0930-1130	**37** 18	0.32±0.02	0.28±0.03 *0.19±0.02*	0.9±0.1	Clouds	~2	~2.5	< 0.1
02/09 1715-1900	**37** 18	0.16±0.01	-	-	-	~0.9	~0.5	< 0.1
Period P₃								
03/09 1400-1540	**70** 70	1.19±0.05	1.21±0.02 *0.65±0.01*	1.43±0.02	Clouds	~5	~1.2	~0.25
04/09 2330-2400	**70** 70	0.84±0.02	-	-	Clouds	~3.5	~1.2	~0.25
05/09 1400-1500	**70** 55	0.92±0.09	-	-	Clouds	~2.8	~1.8	~0.35
06/09 0830-1030	**70** 55	1.33±0.12	1.34±0.06 *0.70±0.05*	1.50±0.04	0.56±0.11	~3.2	~2.8	~0.4
07/09	**70**	1.31±0.11	1.30±0.04	1.46±0.01	0.74±0.03	~3.3	~2.5	~0.3

1600-1900	55		*0.68±0.02*					
08/09 1300-1500	**70** **70**	0.94±0.10	1.87 *1.01*	1.4	0.74±0.08	~3	~1.2	~0.25
09/09 0900-1200	**70** 70	1.04±0.06	1.41±0.09 *0.75±0.01*	1.44±0.01	0.69±0.12	~4	~1	~0.3
11/09 1040-1140	**70** 70	0.70±0.12	0.86 *0.41*	1.68	Clouds	~4.9	~0.8	~0.25

291
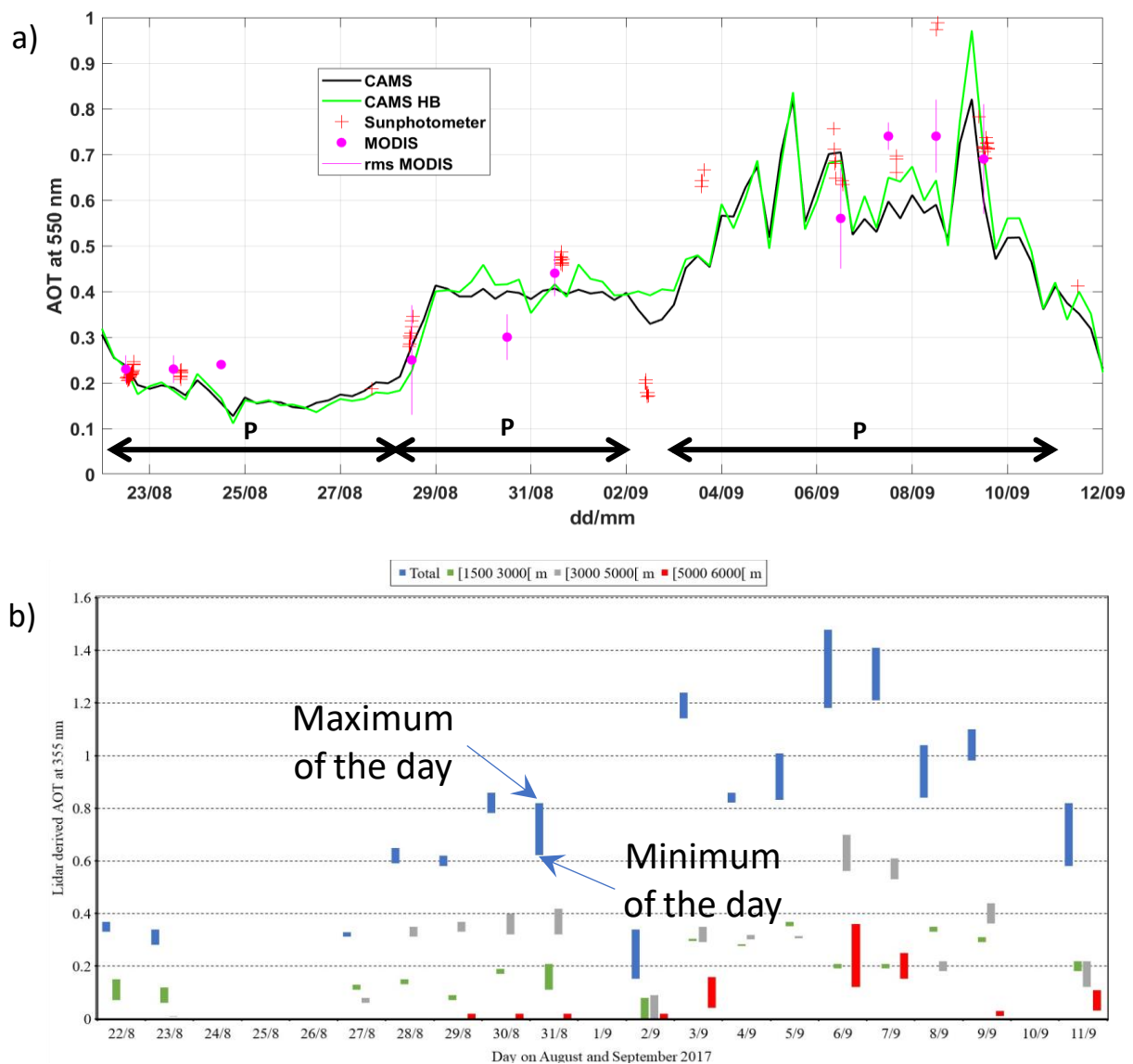
Figure 2: a) Temporal evolution of the AOT at 550 nm derived from CAMS (black and green solid lines), sun photometer (red crosses) and MODIS (magenta dots) data. The green solid line shows CAMS AOT extracted on the grid cell centred on Henties Bay. The black solid line shows the CAMS AOT averaged over 9 grid cells (a 3x3 grid box) centered on

 Henties Bay. The 3 periods highlighted by the AOT values (P₁, P₂ and P₃) are indicated. b) Temporal evolution of the
296 **lidar-derived AOT at 355 nm for the altitude ranges [1500 3000[m in green, [3000 5000[m in grey and [5000 6000[m**
297 **in red. The total AOT is given in blue. The vertical bars delimit the daily extremes of AOT.**

298

299
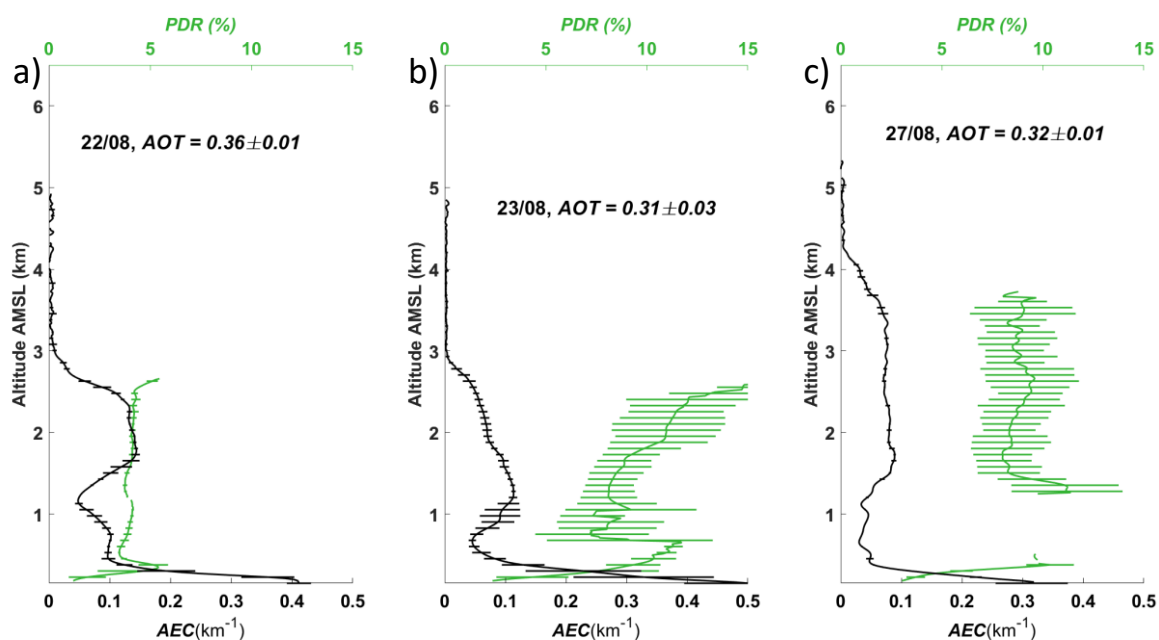
Figure 3: Vertical profiles of the aerosol extinction coefficient (AEC) and particle depolarization ratio (PDR) at 355 nm
301 **with their uncertainties (horizontal bars) for Period P₁: on a) 22 (1400-2300 UTC), b) 23 (1645-2330 UTC) and c) 27**
302 **(1545-1700 UTC). The total aerosol optical thickness at 355 nm (AOT) is also given for each profile with its uncertainty.**

303
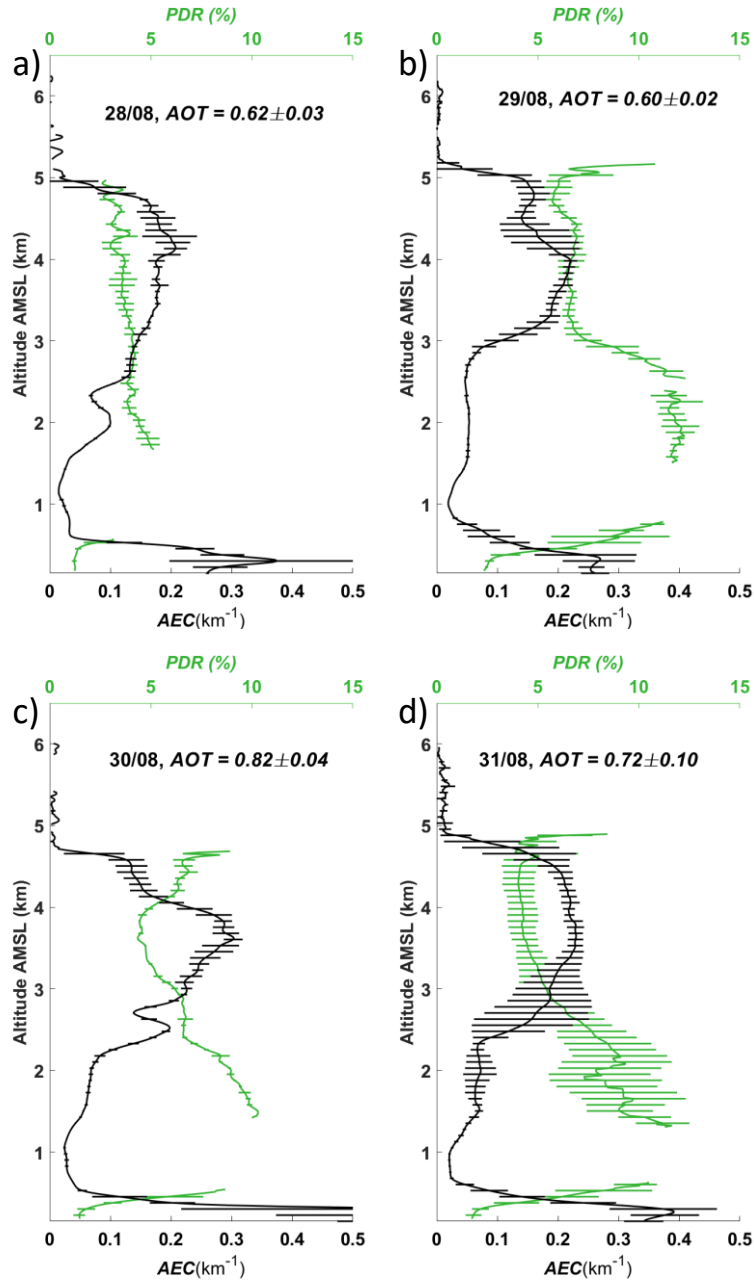
Figure 4: Vertical profiles of the aerosol extinction coefficient (AEC) and particle depolarization ratio (PDR) at 355 nm
with their uncertainties (horizontal bars) for Period P2: on a) 28 (1030-1230 UTC), b) 29 (1730-2250 UTC), c) 30 (1800-
2000 UTC) and d) 31 (1430-2100 UTC) August 2017. The total aerosol optical thickness at 355 nm (AOT) is also given
for each profile with its uncertainty.

308
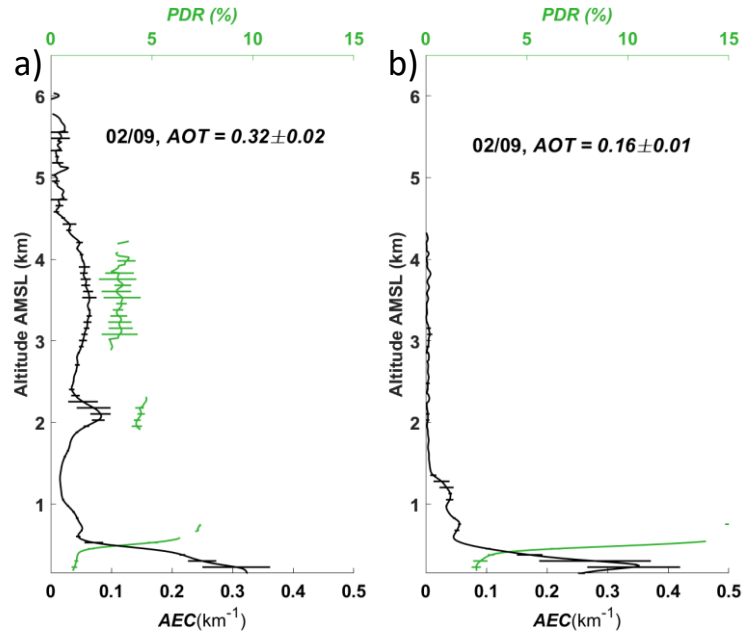
309 **Figure 5: Vertical profiles of the aerosol extinction coefficient (AEC) and particle depolarization ratio (PDR) at 355 nm**
310 **with their uncertainties (horizontal bars) for the transition period on 2 September 2017 at a) 0930-1130 UTC and b)**
311 **1715-1900 UTC. The total aerosol optical thickness at 355 nm (AOT) is also given for each profile with its uncertainty.**

312

313
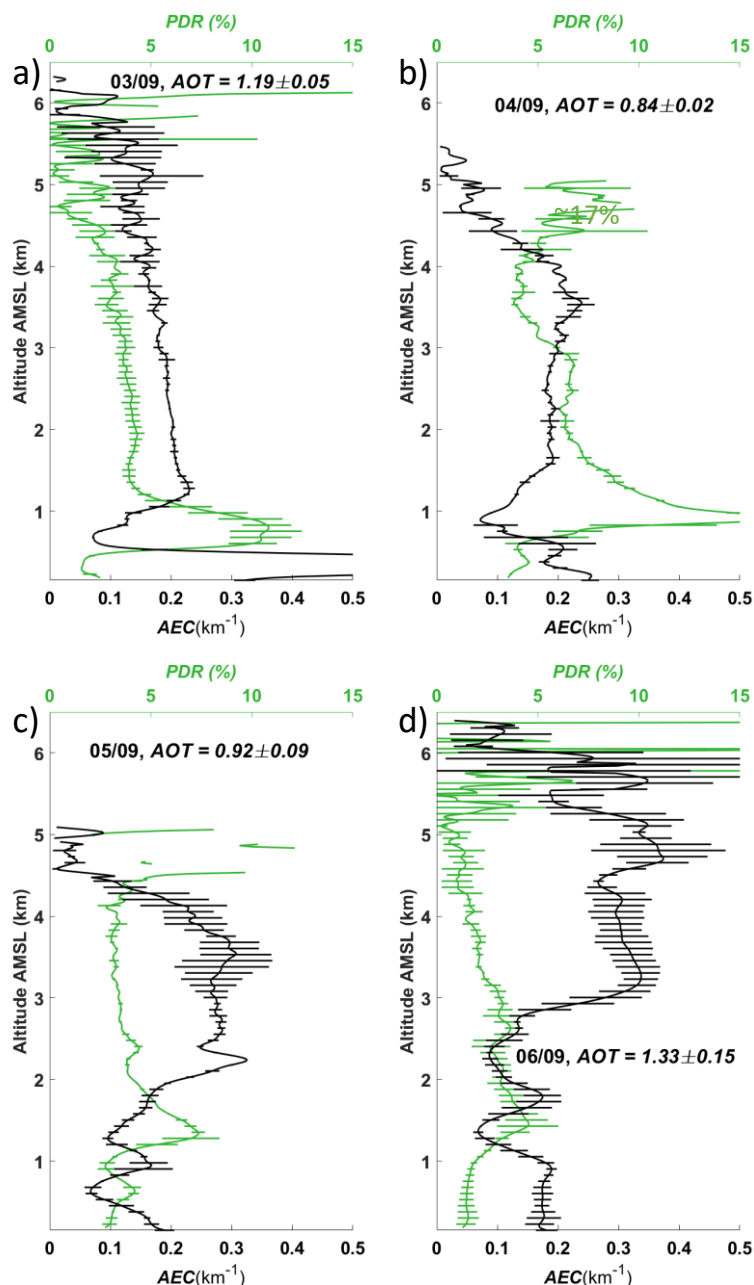
314 **Figure 6: Vertical profiles of the aerosol extinction coefficient (AEC) and particle depolarization ratio (PDR) at 355 nm**
315 **with their uncertainties (horizontal bars) for Period P$_3$: on a) 3 (1400-1540 UTC), b) 4 (2330-2400 UTC), c) 5 (1400-1500**
316 **UTC) and d) 6 (0830-1030 UTC) September 2017. The total aerosol optical thickness at 355 nm (AOT) is also given for**
317 **each profile with its uncertainty.**

318
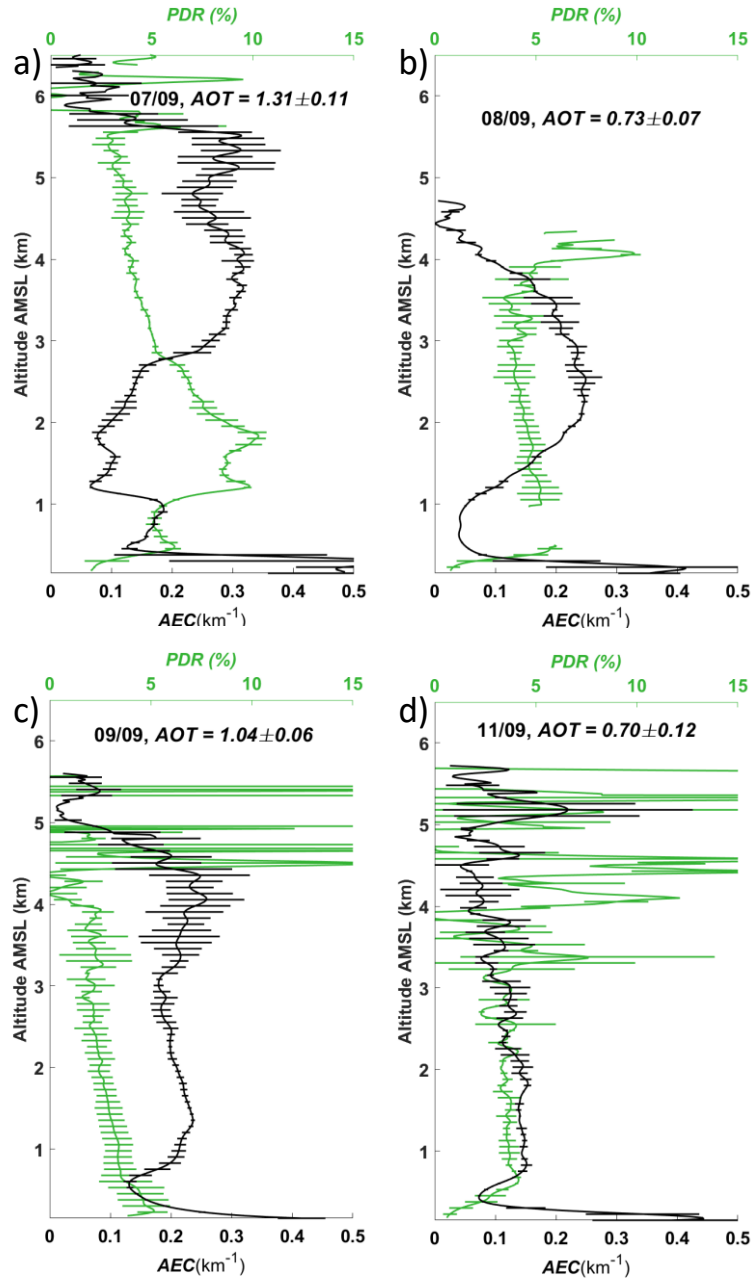
Figure 7: Vertical profiles of the aerosol extinction coefficient (AEC) and particle depolarization ratio (PDR) at 355 nm with their uncertainties (horizontal bars) for Period P₃: on a) 7 (1600-1900 UTC), b) 8 (1300-1500 UTC), c) 9 (0900-1200 UTC) and d) 11 (1040-1140 UTC) September 2017. The total aerosol optical thickness at 355 nm (AOT) is also given for each profile with its uncertainty.

4 Vertical distribution from airborne observations

The purpose of this section is to highlight the spatial variability of the vertical structure of aerosols in the vicinity of Henties Bay through an analysis of the airborne lidar observations acquired offshore during two flights, on 5 and 6 September 2017. Note that airborne observations during AEROCLO-sA were only made during period P₃ (Formenti et al., 2019).

4.1 Flight on 5 Septembre 2017

329   Figure 8a shows the time-space cross section of the LNG-derived apparent aerosol backscatter coefficient (ABC)

330   profiles at 532 nm along the Falcon 20 flight track in the morning of 5 September 2017 following the methodology

331   by Chazette and Totems (2017). LNG data highlight the presence of a widespread elevated BBA layer over the

332   area of interest. The inversion of the LNG ABC data is performed using the same LRs as for the inversion of the

333   ground-based lidar in Henties Bay (70 sr in the FT and 55 sr in the PBL, see Table 3). The average LNG-derived

334   AEC profile shown in Figure 8b is obtained over the ocean between the two vertical dotted black lines in Figure

335   8a around 1000 UTC. Figure 9 shows the comparison between the dropsonde profiles of temperature, wind and

336   relative humidity (RH) located over the ocean in Figure 8a and their counterparts extracted from ERA5 at 1000

337   UTC in a 0.25° x 0.25° grid centred on the Henties Bay site. There is a very good agreement between the vertical

338   wind profiles (intensity and direction), nonetheless the wind is a little stronger on the dropsonde vertical profile,

339   especially around 2 km AMSL, above the marine PBL, where it is in excess of 20 m s^{-1} (and less than 15 m s^{-1} in

340   ERA5). The dropsonde measurements evidence the very sharp RH gradient at the top of the BBA layer (from 80%

341   to nearly 1-2%, Figure 9b) at 6 km AMSL, this gradient being collocated with the large vertical gradient of AEC

342   at 532 nm seen in the LNG data (Figure 8b).). They also evidence a minimum of RH above the PBL, around 2 km

343   AMSL, roughly coinciding with the base of the BBA layer (~2.2 km AMSL, Table 3). The high RH values in the

344   elevated BBA layer may be associated with the large amounts of water vapour released during combustion in wild

345   fires (Clements et al., 2006; Deaconu et al., 2019; Parmar et al., 2008). The high RH may also be characteristic of

346   continental air whereas low humidity air above may be associated with subsiding tropical or mid-latitude air that

347   has been depleted of moisture via prior precipitation. The sharp RH gradient at the top of the BBA layer is not

348   well represented in the ERA5 analysis. The depth of the marine PBL is also seen to be thicker in the observations

349   than in the model (Figure 9b), possibly because the ERA5 profiles is partly over the Namibian coast. The airborne

350   lidar data evidence the presence of stratocumulus over the ocean around 1 km AMSL (Figure 8b, the absence of

351   lidar data below that height indicating that the laser beam is completely extinguished in the cloud), close to the

352   maximum of RH observed with the dropsonde (Figure 9b).

353   When comparing the mean vertical distribution of aerosols from the LNG-derived AEC profile offshore and the

354   ground-based lidar AEC profile in Henties Bay averaged between 1400 and 1500 UTC (Figure 8b, the two profiles

355   being separated by ~100 km), we observe differences in terms of the altitude of the BBA layer top. Note that i)

356   since the two lidars operate at different wavelengths, the AEC intensity is not directly comparable, but the vertical

357   structure of AEC profiles is, and ii) there is a 4-hour difference between the aircraft profiles and the mean profile

358   over Henties Bay. On the other hand, we see that the bottom of the BBA layer is located at roughly the same

359   altitude (Figure 8b). Furthermore, ERA5 analyses also evidence the fact that the dynamical and thermodynamical

360   structure of the lower troposphere over Henties Bay did not evolve significantly between 1000 and 1500 UTC (not

361   shown), except for an increase of RH between 5 and 6 km AMSL (by 20%, coherent with the appearance of clouds

362   as seen in Figure A2c) and of wind speed at 4.5 km AMSL (by 5 m s^{-1}). Rather, the difference may be explained

363   by regional scale circulation in the mid troposphere across the area. Over the ocean, ERA5 data indicates stronger

364   northwest winds (~23 m s^{-1}) at the location of the airborne lidar AEC profile compared to the wind over Henties

365   Bay (12 m s^{-1}) for the entire day on 5 September (not shown). The resulting horizontal wind shear between the

366   Namibian coast and the ocean leads to differential advection within the BBA layer, and a different vertical structure

367   of the aerosol layer between the coastline and over the ocean.

368   **4.2   Flight on 6 Septembre 2017**

369   During the flight on 6 September 2017 (Figure 10a), LNG observations were made further offshore than on the
370   previous day. In Figure 10b, we compare the AEC profiles acquired with LNG to the west and the northwest of
371   Henties Bay (marked '1' and '2', respectively in Figure 10a) at ~0830 and ~0900 UTC, with the average AEC
372   profile obtained between 0700 and 0930 UTC from the ground-based lidar in Henties Bay. Differences in the
373   structure of the BBA layer appear between the vertical profiles west of Henties Bay (profile '1' in Figure 10a) and
374   the one further north (profile '2' in Figure 10a). The shape of the elevated BBA layer observed from the AEC
375   profiles in '1' and in Henties Bay match the structure of the RH and wind speed profiles from the southernmost
376   dropsonde (Figure 11b), with a top (base) altitude of 5 km (3 km) AMSL. The wind in the BBA layer is observed
377   to be rather constant and equal to 17 m s^{-1} on average as well as coming from the north. The maximum RH in the
378   FT is ~55% and observed near the top of the BBA layer (Figure 11b), while small RH values (less than 10%) are
379   seen above ~6 km AMSL. It is worth noting the presence of a slightly enhanced RH layer between 5.5 and 6 km
380   AMSL, where enhanced lidar-derived AEC values are also observed in Henties Bay (Figure 10b). The elevated
381   BBA layer is separated from the PBL by a rather dry layer with small AECs, characterized by a strong wind shear
382   (Figure 11b). The apparent height of the PBL observed in the AEC profile in Henties Bay agrees with the location
383   of the gradient in RH.
384   The AEC profile '2' derived from LNG observations and obtained ~100 km north of profile '1' exhibits a different
385   structure than that of Henties Bay. The top of the BBA layer is observed to be slightly higher (5.2 km AMSL)
386   while the altitude of the base of the BBA layer is the same (~3 km AMSL). The wind speed in the BBA layer as
387   seen from the northernmost dropsonde (Figure 11a) is weaker than when it is off Henties Bay (Figure 11b), while
388   the RH is higher throughout the lower troposphere, especially below the elevated BBA layer. The LNG profile in
389   '2' exhibits significant AEC values below 3 km AMSL corresponding to the base of the BBA layer observed
390   further south, which may be partly related to the impact of RH on aerosol optical properties. A deep moist layer
391   (including the PBL) is observed below the BBA layer.
392   In addition to the important variability in terms of vertical structure of the AEC profiles, it should be noted that
393   the 550 nm AOT derived from the sun photometer in Henties Bay (0.70±0.05) is significantly higher than those
394   determined from the airborne lidar data at 532 nm in '1' (0.37±0.06), but also significantly lower than that
395   measured in '2' (1.13±0.10). This variability also is reflected in the vertical distribution of aerosols above 5 km
396   AMSL, where non-negligible contributions to the AOT are observed in Henties Bay (with $0.15 < AOT < 0.35$ at
397   355 nm, Figure 2b) and in '2' (with $AOT \gtrsim 0.08$ at 532 nm). Such a contribution was even more marked on the
398   previous day in the LNG observations (see Figure 10b), with an AOT at 532 nm above 5 km AMSL in excess of
399   ~0.05.

400
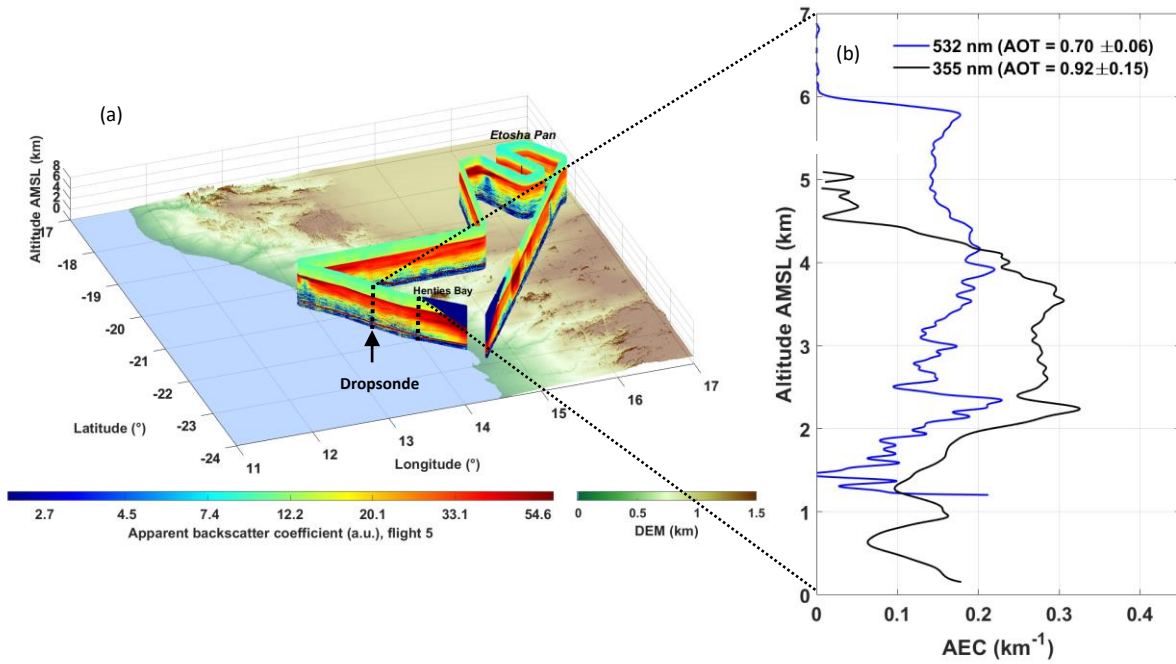
Figure 8: (a) Distance-height ("curtain-like") evolution of the LNG-derived apparent backscatter coefficient at 532 nm below the SAFIRE Falcon 20 during the morning flight on 5 September 2017. The location of the dropsonde released over the ocean is indicated as well as the location of the averaged LNG aerosol extinction coefficient (AEC) profile shown in (b) (between the 2 dotted vertical lines). (b) Vertical profiles of the AEC derived from the airborne lidar at 532 nm (~1000 UTC, blue solid line) and from the ground-based lidar at 355 nm (~1400-1500 UTC, black solid line).

406
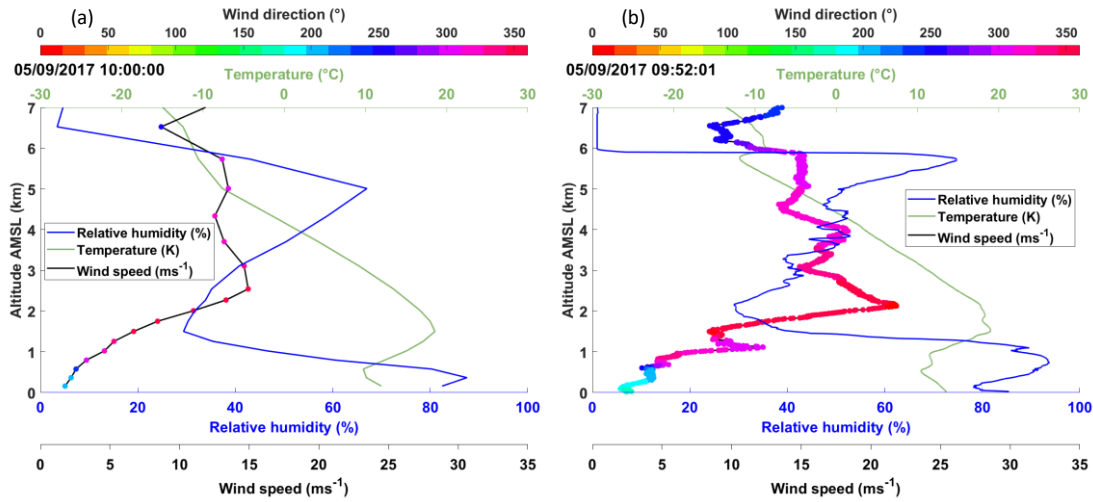
Figure 9: (a) Wind speed (black solid line), wind direction (coloured dots), RH (blue solid line) and temperature (green solid line) profiles extracted from ERA5 at 1000 UTC above Henties Bay over a 0.25° by 0.25° grid. (b) Same as (a) but measured by the dropsonde released over the ocean at 0952 UTC on 5 September 2017.

410
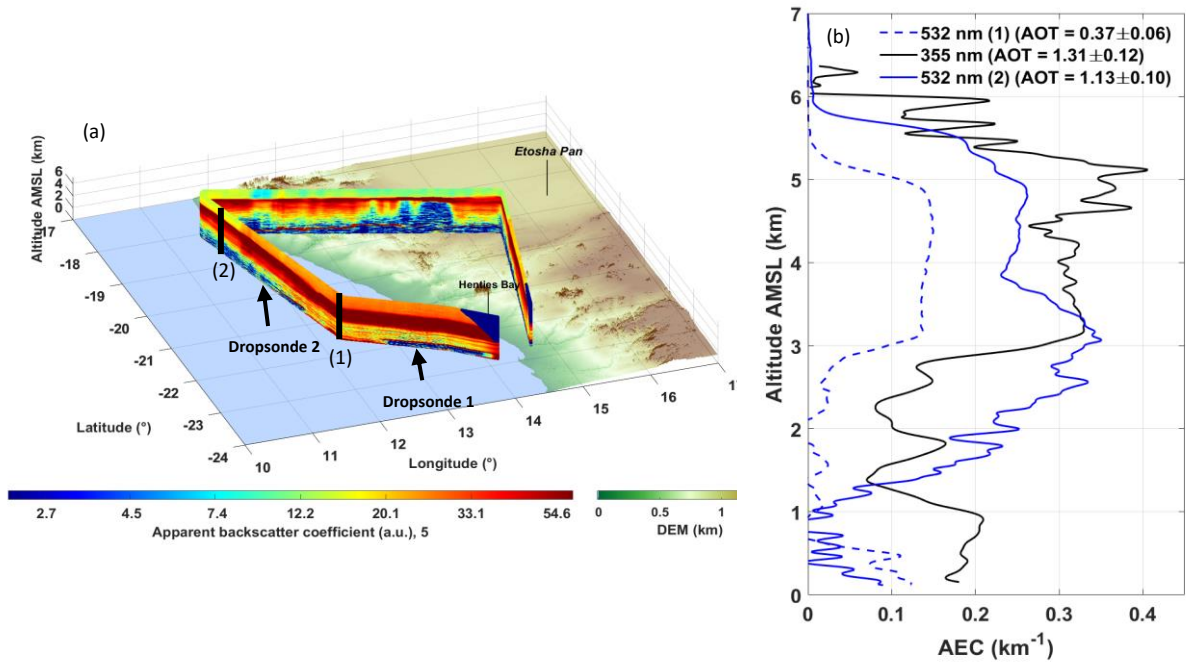
Figure 10: (a) Same as Figure 6a, but on 6 September 2017. The locations of the two launched dropsondes are also indicated by arrows. The lidar AEC profile labelled '1' shown in (b) is obtained after inversion of the LNG observations averaged between the two locations of the two dropsondes. The AEC profile labelled '2' is obtained after inversion of the lidar data between the northern most dropsonde and the northern end of the Falcon leg. (b) Vertical profiles of the AEC derived from the airborne lidar at 532 nm (~0830 and ~0900 UTC, for profile '2' (solid blue line) and '1' (dashed blue line), respectively) and from the ground-based lidar at 355 nm (~0700-0930 UTC, black solid line).

417
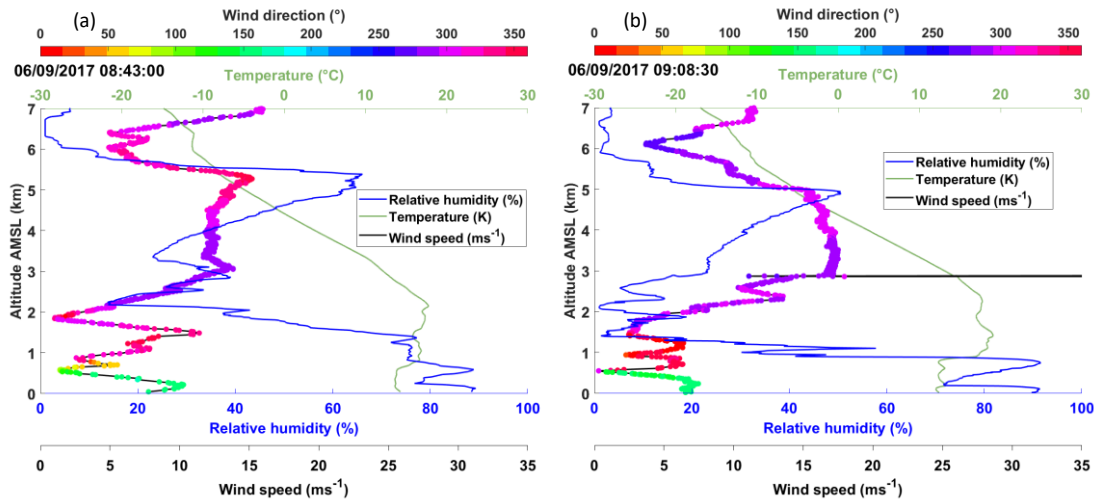
Figure 11: (a) & (b) Same as Figure 7b, but for the dropsondes released at 0843 UTC (to the northwest of Henties Bay, Dropsonde 2 in Figure 10a) and at 0908 UTC (west of Henties Bay, Dropsonde 1 in Figure 10a).

5   Origin of elevated BBA layers over Henties Bay

5.1   RH as indicator of changing synoptic conditions

Figure 12 shows the time-height evolution of hourly RH profiles from ERA5 between 22 August and 9 September 2017 at Henties Bay. The 3 periods (P_1, P_2 and P_3) identified from the AOT (Figure 2) are seen to correspond to distinct RH conditions in the mid troposphere, with rather dry conditions during P_1, then increased RH below 5 km

425 AMSL during P$_2$ and even more humid conditions below 6 km AMSL during P$_3$. For instance, the RH values

426 between 2.5 and 5 km AMSL increases from values below 10% to values in excess of 60% between P$_1$ and P$_2$,

427 which is most probably associated with the transport of BBA over Henties Bay. Likewise, the RH values between

428 5 and 6 km AMSL increases from 5% to ~70-80% between P$_2$ and P$_3$, which is an indication that the meteorology

429 has changed and that the origin of air masses may be different. Periods P$_2$ and P$_3$ are clearly separated by an episode

430 of very dry RH conditions on 2 September, the day also corresponding to a minimum of AOT over Henties Bay

431 (Figure 2). In general, the location of the elevated aerosol layer in the vertical corresponds to the highest RH as

432 previously observed from airborne measurements. In the following, we designed back trajectories analyses to

433 investigate the origin of the air masses in the FT.

434 **5.2   Air masses pathway change during the 3 periods**

435 A statistical study of the back trajectories of air masses originating from Henties Bay was designed to analyse the

436 circulations related to the 3 identified periods P$_1$, P$_2$ and P$_3$. Six-day back-trajectories are initialized at 1200 UTC

437 using the ensemble mode of the Lagrangian HYSPLIT model for which 27 isentropic trajectories are calculated

438 for each selected altitude point over Henties Bay. Altitudes are discretised every 250 m between the base height

439 (~1500 m AMSL) and the maximum top height (~6000 m AMSL) of the BBA layers. A composite of the back

440 trajectories is then made for the 3 different periods by calculating the probability of trajectories passing through

441 each grid point with a spatial resolution of 0.5°. This statistical approach makes it possible to consider the

442 dispersion of back trajectories that can be linked to complex atmospheric circulations. The altitude ranges selected

443 for releasing the back trajectories are derived from the structure of the elevated aerosol layer given in Table 3 and

444 Figures 3-7. They are the same for the 3 periods in order to facilitate comparison: [1500 3000[m AMSL, [3000

445 5000[m AMSL and [5000 6000[m AMSL. To visualize the results, we used the two-dimensional histograms

446 presented in Figures 13-15.

447 **5.2.1   Period P$_1$**

448 During P$_1$, the density of trajectories is highest to the north of Henties Bay, and particularly along the Angolan and

449 Namibian coastlines (Figure 13). The distribution of the trajectories suggests that the aerosols observed over

450 Henties Bay mainly originate from Angola and northern Namibia (close to the back trajectories starting point) and

451 are transported towards the observational super site. Considering the altitude of the back trajectories, plausible

452 injection heights over Angola are highly variable and may reach ~5 km AMSL to explain the vertical structures of

453 lidar profiles. There are also many trajectories coming from over the southern Atlantic Ocean. For the altitude

454 range [3000 5000[m, some trajectories arriving on 25 August in Henties Bay are seen to originate from southern

455 Brazil 6 days earlier, a region where fires are detected by MODIS between 16 and 21 August. It should be noted

456 that BBA would have needed to be injected to heights between 5 and 7 km AMSL in order to be transported to

457 Henties Bay on 25 August. Nevertheless, no lidar measurements are available during this day to confirm this

458 possible alley of cross-Atlantic transport. For the altitude ranges [5000 6000[m no significant aerosol layer is

459 observed by the ground-based lidar (Figure 3).

5.2.2 Period P$_2$

During P$_2$ (Figure 14), the density of trajectories is also high along the Namibia coastline north of Henties Bay between 1500 and 5000 m AMSL and over the ocean. The distribution of trajectories suggests that the BBA observed in Henties Bay mainly are advected within the altitude range [3000 5000[m from central Angola and have travelled a few hundred kilometres over the ocean before being transported back towards the southern African coastline. This constitutes the main contribution of the lidar-derived AEC profiles, provided that the injection heights over Angola can reach 5 km AMSL, as suggested by the CALIOP and CATS observations (see Figure A3). As for P$_1$, we observed no significant aerosol contribution above 5 km AMSL (Figure 4). The contribution from South America are due to air masses arriving over Henties Bay on 30 and 31 August between 3 and 5 km AMSL. These air masses have the possibility to import biomass burning aerosols emitted 6 days before from northern Argentina and injected at altitudes close to 4 km AMSL according to back trajectories. Such injection heights are often observed via CALIOP over South America. The lidar observations over Henties Bay do not show any significant AEC features above 5 km AMSL, in spite of the possibility of cross-Atlantic transport highlighted by the back trajectories. This could be related to a lack of fires in the region overpassed by the trajectories, or injection heights in the biomass burning regions that are below the altitude of the transport associated with the trajectories. It may also be the case that BBA are subject to wet deposition along the trajectories as air masses experience precipitation associated with the weather systems over the Atlantic Ocean.

5.2.3 Period P$_3$

During P$_3$ for the 3 altitude ranges, the occurrence of trajectories (Figure 15) is highest along the northern Namibian coast, over the land. This suggests a more direct transport from the anthropogenic- and/or wild-fire areas in Angola than during P$_2$ and P$_1$, which may explain the highest AOTs for the third period. The occurrence of trajectories over the ocean just west of the southern African coast suggests that a significant part of the aerosols arriving in Henties Bay have travelled over the Atlantic ocean before being transported back towards the continent. This constitutes the main contribution of the lidar-derived AEC profiles below 5 km AMSL, provided that the injection heights over Angola can reach that height over the continent. Above 5 km AMSL, significant AEC features are observed with the lidar (Figure 6 and 7) that reliably contribute to the AOT ((~10-15%, Figure 2b). According to Figure 15c, such features could be related to transport from Angola, provided that BBA are injected sufficiently high over the biomass burning areas. Figure 15c also shows that a significant number of trajectories reaching Henties Bay come from South America. For instance, more trajectories originating from the South America burning zones are also seen over the southern Atlantic Ocean for the altitude range [5000 6000[m than during the two other periods. Several transport pathways from South America to southern Africa are observed for this altitude range: (i) two southern routes where trajectories go as far south as 48°S for the first one and 40°S for the second one before moving equatorward towards Namibia, (ii) a northern routes where trajectories first follow the eastern coast of Brazil before heading due east towards Namibia, and (iii) a more direct eastward route across the Atlantic before turning counter clockwise towards Henties Bay. Back trajectories suggest that air mass transport from South America along the last 3 more northern routes took 5 to 6 days to reach Henties Bay, whereas the transport along the more southern route only took 3-4 days.

5.3 Possible contribution to the AOT from South America during P$_3$

498   We now look specifically at the P_3 period during which a large number of trajectories coming from South America

499   is seen compared with the two other periods. Some of the aerosol layers observed during P_3 between 5 and 6 km

500   AMSL by the ground-based lidar, and in particular those associated with the highest AOTs on 6 and 7 September

501   2017 (Figure 2b), may be associated with biomass burning over Angola, but also with fires occurring on 1-4

502   September 2017 over southern Brazil, northern Argentina and Uruguay.

503   The back trajectories shown in Figures 13-15 are calculated assuming isentropic transport. However, this

504   hypothesis is not necessarily verified during the studied period. Indeed, when trajectories cross the Atlantic Ocean,

505   they encounter more a baroclinic fluid than a barotropic fluid due to the presence of strong low pressure centres

506   such as the cut-off low. The potential temperature is therefore no longer necessarily a tracer of the air mass and

507   isentropic trajectories can quickly diverge towards higher altitudes. This is shown in Figure 16 on 6 September

508   (the same is true on 7 September). Nevertheless, some trajectories pass under 5 km AMSL over northern Argentina.

509   The same trajectory simulation conducted with an isobaric hypothesis on 6 and 7 September shows that all the

510   back-trajectories come from Argentina for altitudes that remain in the range of biomass burning injection heights

511   (~5 km AMSL). However, isobaric trajectories are not necessarily more representative than isentropic trajectories

512   (Stohl, 1998).

513   MODIS-derived AOTs (Figure 17) highlight the existence of an aerosol plume over the ocean along the northern

514   fringe of a large cloud band. The location of fires over South America are also indicated in Figure 17a on 3

515   September 2017. The BBAs seem to be advected across the Atlantic Ocean along two main routes also identified

516   in the previous back trajectory analyses (Section 5.2.3). The northernmost one follows the coast of Brazil before

517   heading straight towards Namibian coasts. The poleward one follows the strong winds at 500 hPa along the western

518   flank of a high pressure centred over the eastern coast of Brazil (Figure 17a). A mid-tropospheric westerly jet then

519   transports the aerosol plumes over the Atlantic Ocean where they are then advected northward around the eastern

520   edge of the high-pressure system located over the Atlantic Ocean. The ubiquitous cloud cover along the southern

521   and eastern fringes of the high-pressure system does not allow the retrieval of AOTs with MODIS, except offshore

522   of the Rio de la Plata estuary and at the edge of cloud fields caught in the west-east circulation. The northward

523   progression of the air masses transporting the BBA along the coast is further accelerated by the presence of a

524   poleward moving cut-off low (centred at 40°S, 15°W) separating from the westerlies further south (Figure 17a).

525   Over the following days, the cut-off low is seen to merge back with the westerlies while progressing eastward, and

526   the high-pressure system at 500 hPa is observed to also move over the Atlantic Ocean and merge with the St

527   Helena high on 5 September (Figure 17b). The mid-tropospheric westerly jet may transport the aerosols issued

528   from biomass burning over South America along the southern fringe of the St Helena high, which is centred at

529   ~25°S and ~20°W. The jet is seen to extend quite far east over the Atlantic Ocean and to almost reach the southern

530   tip of southern Africa (Figure 17c). Some aerosols travelling along the southern route may be redirected towards

531   Namibia by the strong northerly flow along the eastern flank of the St Helena high.

532   Furthermore, the temporal variability of BBA transport patterns from South America to southern Africa may be

533   related to the variability of the Southern Annular Mode (SAM, i.e. the north-south movement of the westerly wind

534   belt around Antarctica). Indeed, Trenberth (2002) show that the SAM is the main driver of extratropical circulation

535   in the Southern Hemisphere on weekly to decennial time scales, which is also the main driver of climate variability,

536   affecting anthropogenic- and/or wild-fire activities over South America (e.g. Holz et al., 2017). For instance,

537   positive phases of the SAM (i.e. when a band of westerly winds contracts toward Antarctica) are associated

538 primarily with warm conditions in the forested areas of South America, thereby favouring biomass burning events.
539 On the other hand, negative phases lead to an expansion of the wind belt towards the lower latitudes, leading to
540 the possibility for BBA transported in the westerlies to reach southern Africa in the austral winter. Given the
541 possible short time scale of variability of the SAM, it is likely that the transport patterns to Henties Bay identified
542 during period P_3 are related to a negative SAM phase, while during P_1 they are related to a positive phase. On
543 longer time scales, climate modelling studies indicate a robust positive trend in the SAM for the end of this century
544 (Lim et al., 2016), so that climate conditions conducive to an impact of the widespread South American fire activity
545 in southern Africa will likely continue throughout the 21st century. . However, further studies are needed to support
546 this conclusion, which will have to be based on longer observation periods involving lidar technology.
547
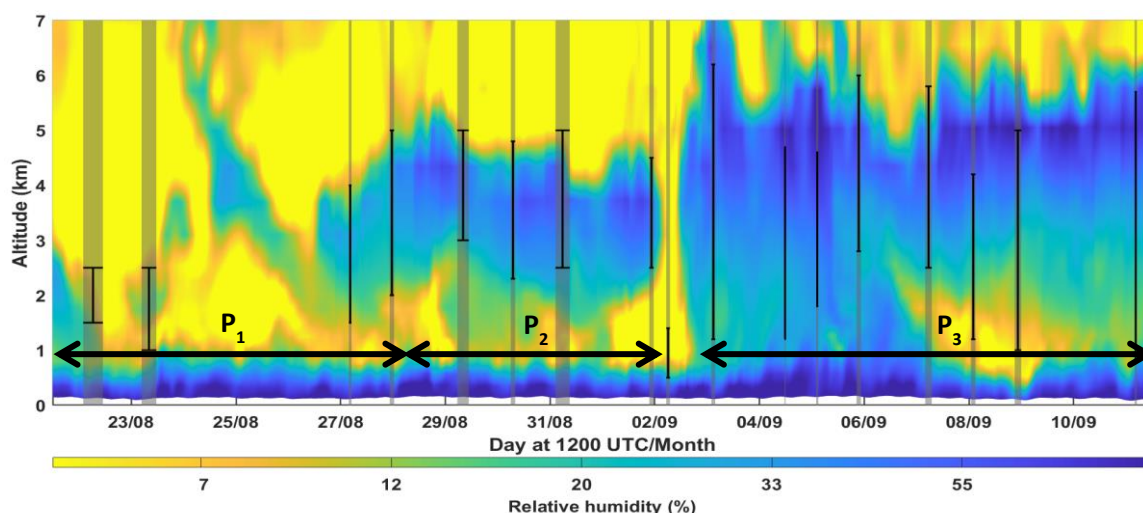
549 **Figure 12: Time-height evolution of the relative humidity vertical profiles derived from ERA5 above Henties Bay. The**
550 **grey vertical lines indicate the time of the ground-based lidar profiles shown in Figure 3-7. The thickness of the grey**
551 **lines depends on the averaging period (the thicker the line, the longer the average). The 3 periods highlighted by the**
552 **AOT values (P_1, P_2 and P_3) are also indicated. The vertical black lines show the lidar-derived altitude location of the**
553 **aerosol layer.**

554
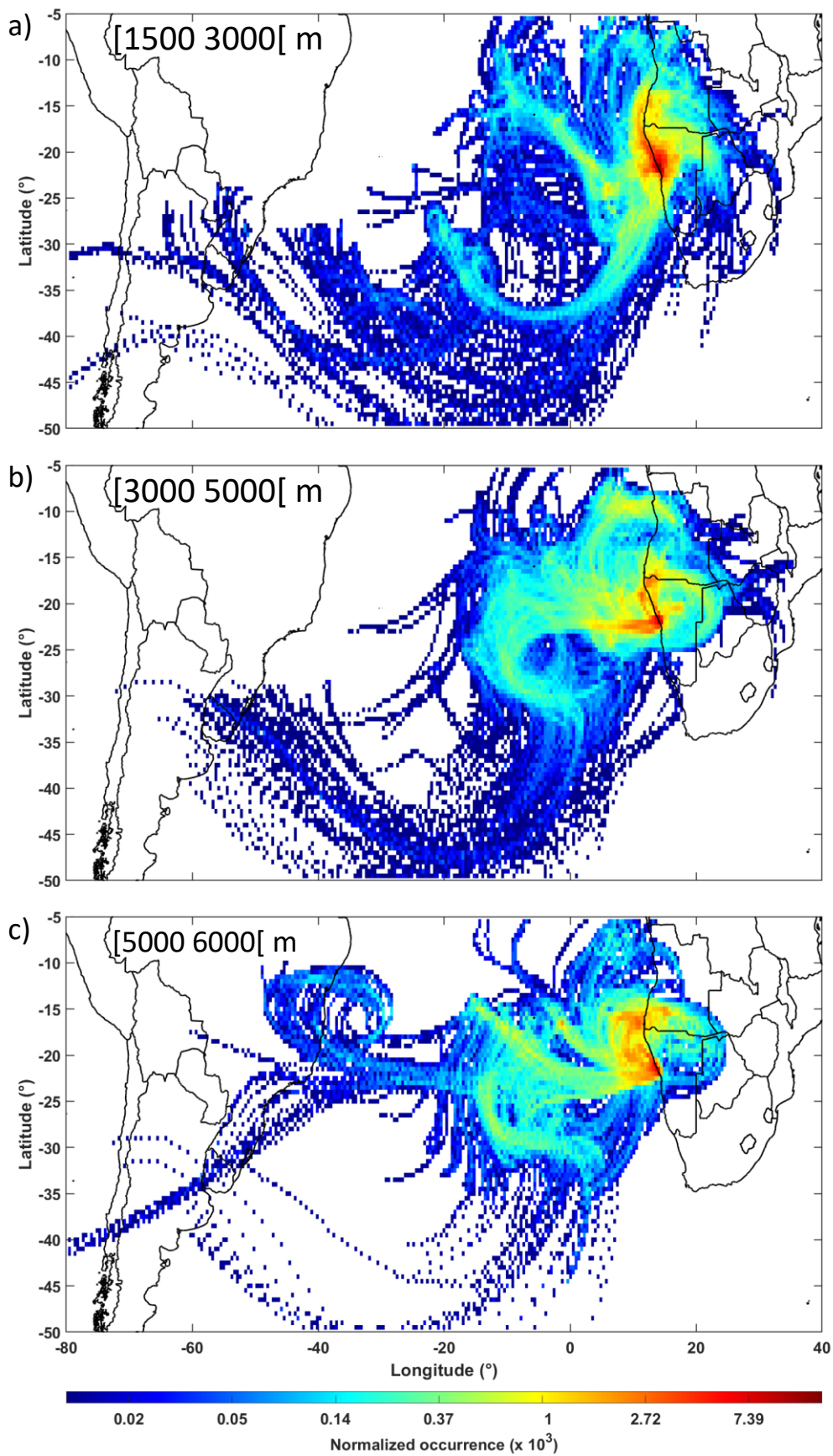
555   **Figure 13: Normalized occurrence of the back trajectories starting over Henties Bay at 1200 UTC during periods P₁,**
556   **from the altitude range [1500 3000[(a) [3000 5000[(b) and [5000 6000[(c), m. The calculations have been made using**

557   **6-day isentropic back trajectories with the HYSPLIT model (courtesy of NOAA Air Resources Laboratory;**
558   **http://www.arl.noaa.gov) in ensemble mode. The normalization is performed with respect to the total number of pixels**
559   **for a horizontal resolution of 0.5°.**
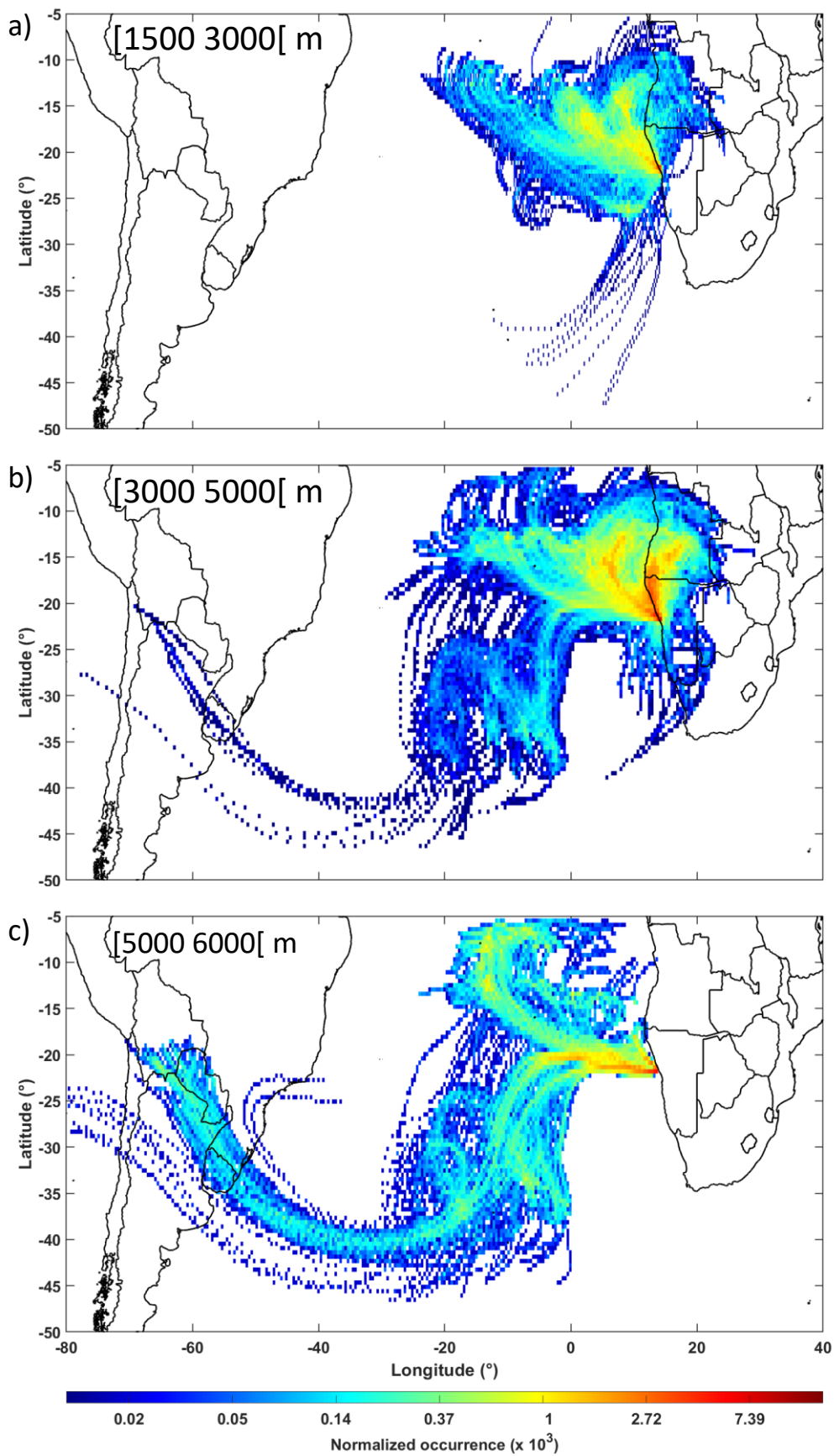
561   **Figure 14: Normalized occurrence of the back trajectories starting over Henties Bay at 1200 UTC during periods P₂,**
562   **from the altitude range [1500 3000[(a) [3000 5000[(b) and [5000 6000[(c), m. The calculations have been made using**
563   **6-day isentropic back trajectories with the HYSPLIT model (courtesy of NOAA Air Resources Laboratory;**
564   **http://www.arl.noaa.gov) in ensemble mode. The normalization is performed with respect to the total number of pixels**
565   **for a horizontal resolution of 0.5°.**

566
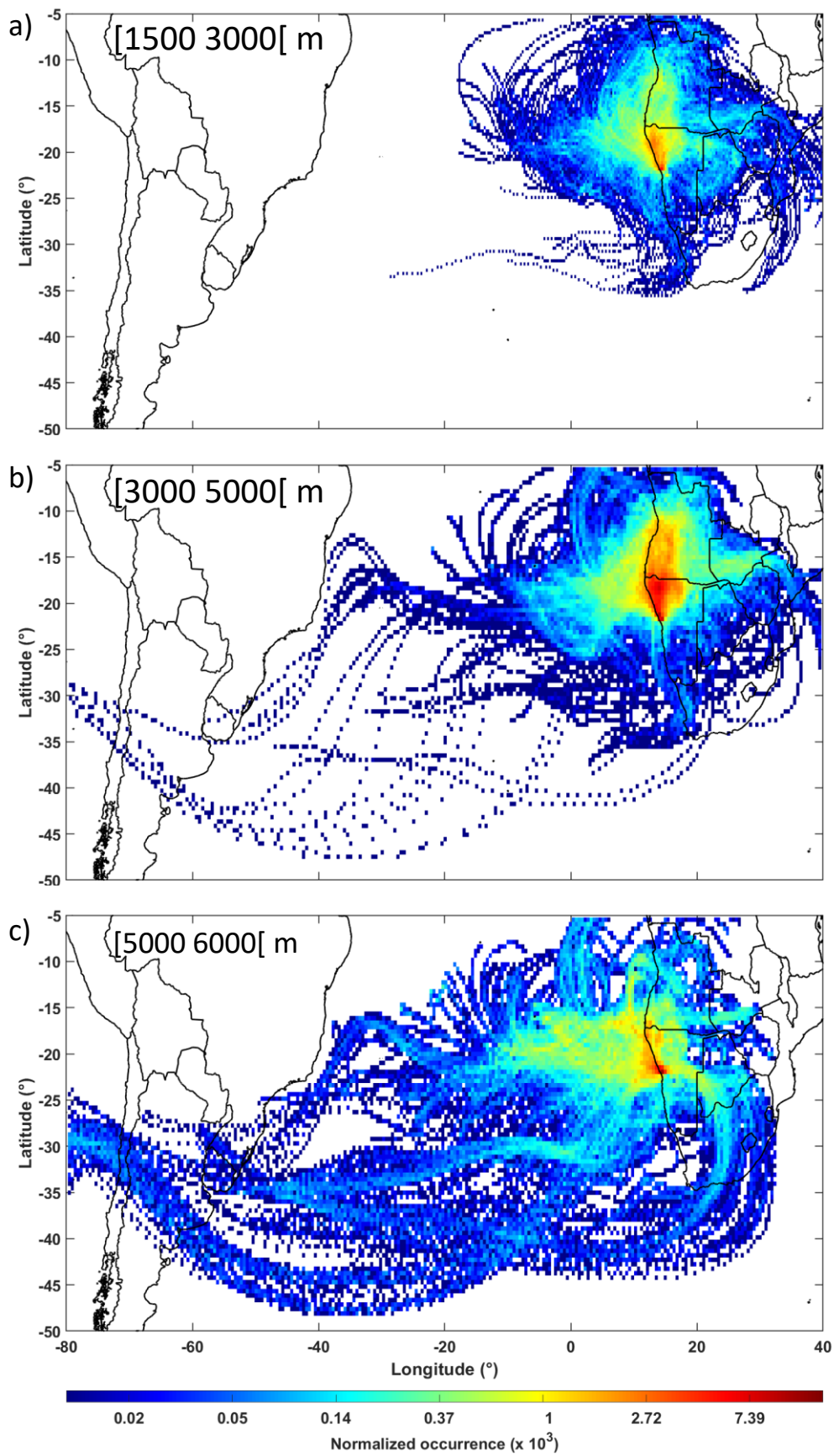
Figure 15: Normalized occurrence of the back trajectories starting over Henties Bay at 1200 UTC during periods P$_3$, from the altitude range [1500 3000[(a) [3000 5000[(b) and [5000 6000[(c), m. The calculations have been made using 6-day isentropic back trajectories with the HYSPLIT model (courtesy of NOAA Air Resources Laboratory; http://www.arl.noaa.gov) in ensemble mode. The normalization is performed with respect to the total number of pixels for a horizontal resolution of 0.5°.
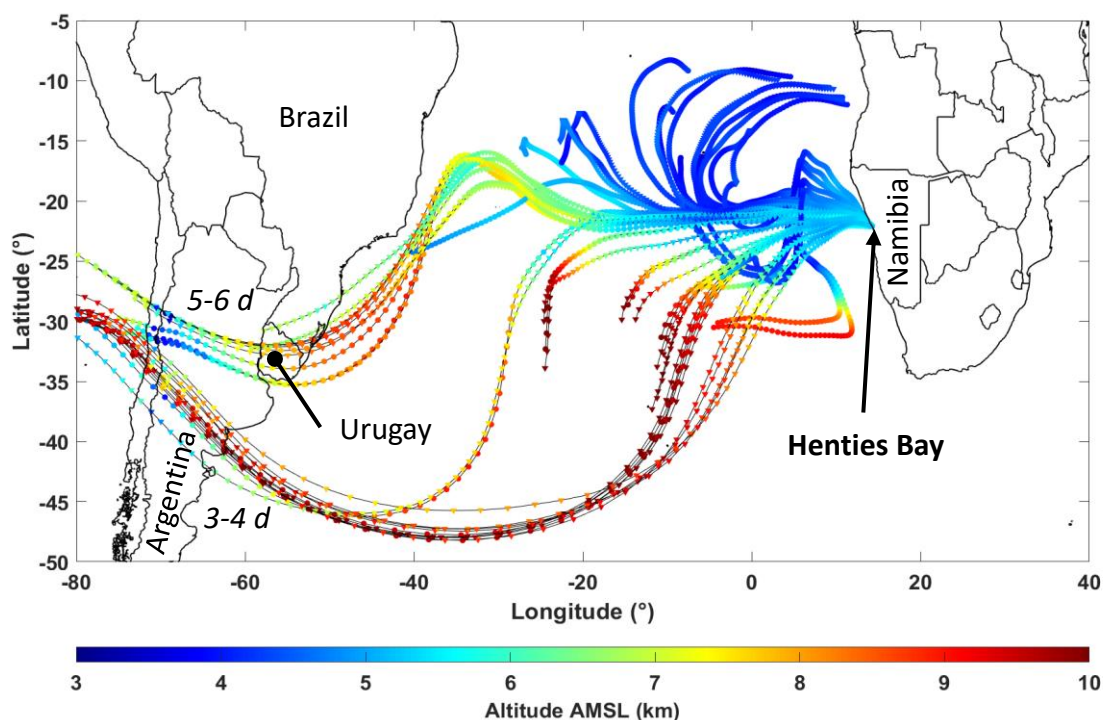
Figure 16: 6-days isentropic back trajectories starting over Henties Bay on 6 September at 1200 UTC. They are computed by the HYSPLIT model (courtesy of NOAA Air Resources Laboratory; http://www.arl.noaa.gov) in ensemble mode. The time to arrival above the South America is indicated. The altitude of back trajectories along the route is given by the colour bar.

577
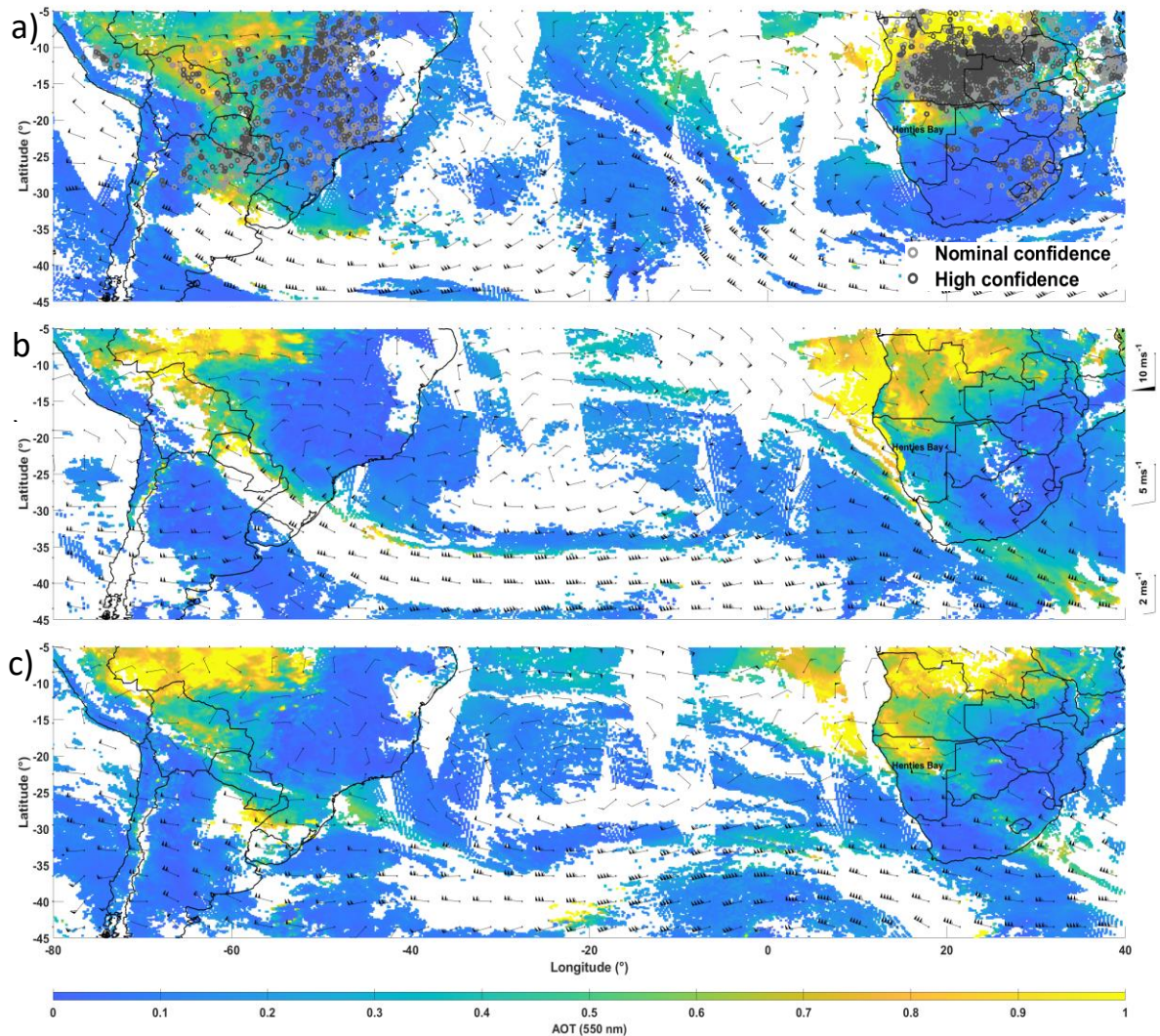
Figure 17: MODIS-derived AOT at 550 nm on (a) on 3 September 2017 with wild fire hotspots over both South Africa and South America, (b) on 5 September 2017 and c) 6 September 2017. The ERA5 wind field at 500 hPa on each day have been added in black.

6   Conclusion

During the intensive field campaign of the AEROCLO-sA project (22 August - 12 September 2017), the very persistent cloud cover topping the marine boundary did not allow continuous ground-based monitoring of the aerosol layers above the stratocumulus deck, in the mid-troposphere. Nevertheless, the available lidar observations performed over the coastal site of Henties Bay allowed to highlight three contrasted periods of biomass burning aerosol transport (P_1, P_2 and P_3). The inversion of the ground-based lidar profiles was carried out using the constraints provided by the aerosol typing of the CALIOP and CATS space-borne instruments, but also the photometric measurements from AERONET network. The latter showed an overall good agreement with the MODIS AOT observations and the AOT outputs of the CAMS model. Differences were noted in the presence of high aerosol contents (AOT at 355 nm > 0.8) between the lidar- and sun photometrer-derived AOTs, but those were likely due to the presence of clouds that were not detected by the passive sensors.

592   Combining observations and back trajectory analyses, we highlight the existence of 3 periods with very different

593   transport modes towards Henties Bay during the field campaign. The lowest AOTs (<0.2 at 550 nm) of the first

594   period (P_1) are associated with air masses from Angola travelling along the Namibian and Angolan coasts.

595   Intermediate AOTs (~0.4 at 550 nm) of the second period (P_2) are associated with polluted dusts (i.e. dust mixed

596   with biomass burning aerosols from Angola), as well as dust from the Etosha Pan, which are recirculated above

597   the ocean. During the third period (P_3), the largest AOTs (~0.7 at 550 nm) are observed, mainly due to a more

598   direct transport from the Angola burning areas with an aerosol plume vertical extending between 1.5 and ~6 km

599   AMSL. The atmospheric composition in the free troposphere for this period is the most variable in the time. We

600   show a possible contribution of forest fire aerosols from South America (South of Brazil, Argentina and Uruguay)

601   with plumes transported to Henties Bay around 5000-6000 m AMSL and mainly observed on 6 and 7 September

602   with a contribution to the total AOT of ~10-15%. The aerosol plume from South America could be advected across

603   the Atlantic Ocean along a route following the strong westerlies of the southern fringes of the St Helena high

604   before heading north toward Namibia in connection with an equatorward moving cut-off low.

605   To the authors' knowledge, this is the first time that the evolution of the optical properties of aerosols in the FT

606   over coastal Namibia is characterized, in relation to different transport regimes. The main contribution of the BBA

607   from Angola and the arguably smaller contribution of the South American anthropogenic- and/or wild-fires to the

608   atmospheric aerosol composition over the Namibian coast were shown. The synergy between active and passive

609   remote sensing observations performed from ground-based and space-borne platforms together with back

610   trajectory analyses, was essential to provide these conclusions. In particular, the transport of BBA from South

611   America and its likely advection on top of the BBA layers originating from Angola and northeast Namibia could

612   be climatically significant in this region of the globe, where the feedback of aerosols and clouds on the radiative

613   balance of the Earth system is still poorly known.

614

615   **Acknowledgments.** This work was supported by the French National Research Agency under grant agreement n°

616   ANR-15-CE01-0014-01, the French national program LEFE/INSU, the Programme national de Télédetection

617   Spatiale (PNTS, http://www.insu.cnrs.fr/pnts), grant n° PNTS-2016-14, the French National Agency for Space

618   Studies (CNES), and the South African National Research Foundation (NRF) under grant UID 105958. The

619   authors would also like to thank the AERIS data center for their support during the campaign and managing the

620   AEROCLO-sA database. The research leading to these results has received funding from the European Union's

621   7th Framework Programme (FP7/2014-2018) under EUFAR2 contract n°312609". Airborne data was obtained

622   using the aircraft managed by SAFIRE, the French facility for airborne research, an infrastructure of the French

623   National Center for Scientific Research (CNRS), Météo-France and the French National Center for Space Studies

624   (CNES). The authors would like to thank F. Blouzon and A. Abchiche (DT-INSU) as well as P. Genau and M. van

625   Haecke (LATMOS) for their support in operating and processing the LNG data. The invaluable diplomatic

626   assistance of the French Embassy in Namibia, the administrative support of the Service Partnership and

627   Valorisation of the Regional Delegation of the Paris-Villejuif Region of the CNRS, and the cooperation of the

628   Namibian National Commission on Research, Science and Technology (NCRST) are sincerely acknowledged. The

629   long-term hosting and support of the SANUMARC, a research center of the University of Namibia in Henties Bay

630   have been essential through the years and are warmly appreciated. The authors acknowledge the MODIS science,

631   processing and data support teams for producing and providing MODIS data (at

632 https://modis.gsfc.nasa.gov/data/dataprod/) and the NASA Langley Research Center Atmospheric Sciences Data

633 Center for the data processing and distribution of CALIPSO products (level 4.10, at

634 https://eosweb.larc.nasa.gov/HORDERBIN/HTML_Start.cgi). The authors would like to thank the AERONET

635 network for sun photometer products (at https://aeronet.gsfc.nasa.gov/). Finally, the authors are grateful to Michael

636 Diamond and an anonymous reviewer for their comments that helped improve the overall quality of the paper.

637

638 **Data availability.** The aircraft and ground-based data used here can be accessed using the AEROCLO-sA database

639 at http://baobab.sedoo.fr/AEROCLO-sA/. An embargo period of 2 years after the upload applies. After that,

640 external users can access the data in the same way as AEROCLO-sA participants before that time. Before the end

641 of the embargo period, external users can request the release of individual datasets. It is planned for AEROCLO-

642 sA data to get DOIs, but this has not been carried out for all datasets yet. The back trajectories data can be obtained

643 upon request to the first author of the paper.

644 **Author contributions.** PC inverted the ground-based and airborne lidar data, analyzed the data and wrote the

645 paper, with comments from all the co-authors; CF analyzed the data and wrote the paper; JT aligned and validated

646 the ground-based lidar, MG participated to the study of atmospheric dynamic and to the paper editing, GS

647 participated to the back-trajectories computation, AB gathered the CATS lidar data and the wind fields, PF

648 coordinated the AEROCLO-sA project, XL participated in the pre- and post-field calibration and operation of the

649 lidar, KD and JFD maintained and operated the lidar during the field campaign.

650 **Competing interests.** The authors declare that they have no conflict of interest.

651 **Special issue statement.** This article is part of the special issue "New observations and related modeling studies

652 of the aerosol–cloud–climate system in the Southeast Atlantic and southern Africa regions" (ACP/AMT inter-

653 journal SI)". It is not associated with a conference.

654 **7 References**

655 Ackerman, A. S., Toon, O. B., Stevens, D. E., Heymsfield, A. J., Ramanathan, V. and Welton, E. J.: Reduction of
656 tropical cloudiness by soot, Science, 288(5468), 1042–7, doi:10.1126/SCIENCE.288.5468.1042, 2000.
657 Adebiyi, A. A. and Zuidema, P.: The role of the southern African easterly jet in modifying the southeast Atlantic
658 aerosol and cloud environments, Q. J. R. Meteorol. Soc., 142(697), 1574–1589, doi:10.1002/qj.2765, 2016.
659 Adebiyi, A. A., Zuidema, P. and Abel, S. J.: The convolution of dynamics and moisture with the presence of
660 shortwave absorbing aerosols over the southeast Atlantic, J. Clim., 28(5), 1997–2024, doi:10.1175/JCLI-D-14-
661 00352.1, 2015.
662 Andreae, M. O., Elbert, W. and de Mora, S. J.: Biogenic sulfur emissions and aerosols over the tropical South
663 Atlantic: 3. Atmospheric dimethylsulfide, aerosols and cloud condensation nuclei, J. Geophys. Res., 100(D6),
664 11335, doi:10.1029/94jd02828, 2004.
665 Ångström, A.: The parameters of atmospheric turbidity, Tellus A, 16, 64–75, doi:10.3402/tellusa.v16i1.8885,
666 1964.
667 Bates, T. S., Quinn, P. K., Coffman, D. J., Johnson, J. E., Miller, T. L., Covert, D. S., Wiedensohler, A., Leinert,
668 S., Nowak, A. and Neusüss, C.: Regional physical and chemical properties of the marine boundary layer aerosol
669 across the Atlantic during Aerosols99: An overview, J. Geophys. Res. Atmos., 106(D18), 20767–20782,
670 doi:10.1029/2000JD900578, 2001.
671 Bruneau, D., Pelon, J., Blouzon, F., Spatazza, J., Genau, P., Buchholtz, G., Amarouche, N., Abchiche, A. and
672 Aouji, O.: 355-nm high spectral resolution airborne lidar LNG: system description and first results, Appl. Opt.,
673 54(29), 8776, doi:10.1364/AO.54.008776, 2015.

674 Burton, S. P., Ferrare, R. A., Hostetler, C. A., Hair, J. W., Rogers, R. R., Obland, M. D., Butler, C. F., Cook, A.
675 L., Harper, D. B. and Froyd, K. D.: Aerosol classification using airborne High Spectral Resolution Lidar
676 measurements – methodology and examples, Atmos. Meas. Tech., 5(1), 73–98, doi:10.5194/amt-5-73-2012, 2012.
677 Chazette, P.: The monsoon aerosol extinction properties at Goa during INDOEX as measured with lidar, J.
678 Geophys. Res., 108(D6), 4187, doi:10.1029/2002JD002074, 2003.
679 Chazette, P. and Totems, J.: Mini N2-Raman Lidar onboard ultra-light aircraft for aerosol measurements:
680 Demonstration and extrapolation, Remote Sens., 9(12), doi:10.3390/rs9121226, 2017.
681 Chazette, P., Bocquet, M., Royer, P., Winiarek, V., Raut, J. C., Labazuy, P., Gouhier, M., Lardier, M. and Cariou,
682 J. P.: Eyjafjallajökull ash concentrations derived from both lidar and modeling, J. Geophys. Res. Atmos., 117,
683 doi:10.1029/2011JD015755, 2012a.
684 Chazette, P., Dabas, a., Sanak, J., Lardier, M. and Royer, P.: French airborne lidar measurements for
685 Eyjafjallajökull ash plume survey, Atmos. Chem. Phys., 12(15), 7059–7072, doi:10.5194/acp-12-7059-2012,
686 2012b.
687 Chazette, P., Totems, J., Ancellet, G., Pelon, J. and Sicard, M.: Temporal consistency of lidar observables during
688 aerosol transport events in the framework of the ChArMEx/ADRIMED campaign at Menorca Island in June 2013,
689 Atmos. Chem. Phys. Discuss., 15(22), 32723–32757, doi:10.5194/acpd-15-32723-2015, 2015.
690 Chew, B. N., Campbell, J. R., Reid, J. S., Giles, D. M., Welton, E. J., Salinas, S. V. and Liew, S. C.: Tropical
691 cirrus cloud contamination in sun photometer data, Atmos. Environ., 45(37), 6724–6731,
692 doi:10.1016/j.atmosenv.2011.08.017, 2011.
693 Clements, C. B., Potter, B. E. and Zhong, S.: In situ measurements of water vapor, heat, and CO2 fluxes within a
694 prescribed grass fire, Int. J. Wildl. Fire, 15(3), 299, doi:10.1071/WF05101, 2006.
695 Deaconu, L. T., Ferlay, N., Waquet, F., Peers, F., Thieuleux, F. and Goloub, P.: Satellite inference of water vapor
696 and aerosol-above-cloud combined effect on radiative budget and cloud top processes in the Southeast Atlantic
697 Ocean, Atmos. Chem. Phys. Discuss., 1–34, doi:10.5194/acp-2019-189, 2019.
698 Dee, D. P., Uppala, S. M., Simmons, A. J., Berrisford, P., Poli, P., Kobayashi, S., Andrae, U., Balmaseda, M. A.,
699 Balsamo, G., Bauer, P., Bechtold, P., Beljaars, A. C. M., van de Berg, L., Bidlot, J., Bormann, N., Delsol, C.,
700 Dragani, R., Fuentes, M., Geer, A. J., Haimberger, L., Healy, S. B., Hersbach, H., Hólm, E. V, Isaksen, L.,
701 Kållberg, P., Köhler, M., Matricardi, M., Mcnally, A. P., Monge-Sanz, B. M., Morcrette, J. J., Park, B. K., Peubey,
702 C., de Rosnay, P., Tavolato, C., Thépaut, J. N. and Vitart, F.: The ERA-Interim reanalysis: Configuration and
703 performance of the data assimilation system, Q. J. R. Meteorol. Soc., 137(656), 553–597, 2011.
704 Diamond, M. S., Dobracki, A., Freitag, S., Small Griswold, J. D., Heikkila, A., Howell, S. G., Kacarab, M. E.,
705 Podolske, J. R., Saide, P. E. and Wood, R.: Time-dependent entrainment of smoke presents an observational
706 challenge for assessing aerosol–cloud interactions over the southeast Atlantic Ocean, Atmos. Chem. Phys., 18(19),
707 14623–14636, doi:10.5194/acp-18-14623-2018, 2018.
708 Dieudonné, E., Chazette, P., Marnas, F., Totems, J. and Shang, X.: Raman Lidar Observations of Aerosol Optical
709 Properties in 11 Cities from France to Siberia, Remote Sens., 9(10), 978, doi:10.3390/rs9100978, 2017.
710 Draxler, R. R. R. and Rolph, G. D. D.: HYSPLIT (HYbrid Single-Particle Lagrangian Integrated Trajectory) Model
711 access via NOAA ARL READY Website (http://www.arl.noaa.gov/HYSPLIT.php). NOAA Air Resources
712 Laboratory, College Park, MD., NOAA Air Resour. Lab. [online] Available from:
713 http://ready.arl.noaa.gov/HYSPLIT_ash.php, 2014.
714 Dubovik, O., Smirnov, A., Holben, B. N., King, M. D., Kaufman, Y. J., Eck, T. F. and Slutsker, I.: Accuracy
715 assessments of aerosol optical properties retrieved from Aerosol Robotic Network (AERONET) Sun and sky
716 radiance measurements, J. Geophys. Res. Atmos., 105(D8), 9791–9806, doi:10.1029/2000JD900040, 2000.
717 Flamant, C., Pelon, J., Chazette, P. and Trouillet, V.: Marine aerosol vertical distribution retrieval using airborne
718 backscatter lidar measurements, J. Aerosol Sci., 29(SUPPL.2), 1998.
719 Formenti, P., Piketh, S. J., Namwoonde, A., Klopper, D., Burger, R., Cazaunau, M., Feron, A., Gaimoz, C.,
720 Broccardo, S., Walton, N., Desboeufs, K., Siour, G., Hanghome, M., Mafwila, S., Omoregie, E., Junkermann, W.
721 and Maenhaut, W.: Three years of measurements of light-absorbing aerosols over coastal Namibia: seasonality,
722 origin, and transport, Atmos. Chem. Phys., 18(23), 17003–17016, doi:10.5194/acp-18-17003-2018, 2018.
723 Formenti, P., D'Anna, B., Flamant, C., Mallet, M. D., Piketh, S. J., Schepanski, K., Waquet, F., Auriol, F.,
724 Brogniez, G., Burnet, F., Chaboureau, J.-P., Chauvigné, A., Chazette, P., Denjean, C., Desboeufs, K., Doussin, J.-
725 F., Elguindi, N., Feuerstein, S., Gaetani, M., Giorio, C., Klopper, D., Mallet, M. D., Nabat, P., Monod, A., Solmon,
726 F., Namwoonde, A., Chikwililwa, C., Mushi, R., Welton, E. J., Holben, B., Formenti, P., D'Anna, B., Flamant, C.,
727 Mallet, M. D., Piketh, S. J., Schepanski, K., Waquet, F., Auriol, F., Brogniez, G., Burnet, F., Chaboureau, J.-P.,
728 Chauvigné, A., Chazette, P., Denjean, C., Desboeufs, K., Doussin, J.-F., Elguindi, N., Feuerstein, S., Gaetani, M.,
729 Giorio, C., Klopper, D., Mallet, M. D., Nabat, P., Monod, A., Solmon, F., Namwoonde, A., Chikwililwa, C.,
730 Mushi, R., Welton, E. J. and Holben, B.: The Aerosols, Radiation and Clouds in southern Africa (AEROCLO-sA)
731 field campaign in Namibia: overview, illustrative observations and way forward, Bull. Am. Meteorol. Soc.,
732 BAMS-D-17-0278.1, doi:10.1175/BAMS-D-17-0278.1, 2019.
733 Fuchs, J., Cermak, J., Andersen, H., Hollmann, R. and Schwarz, K.: On the Influence of Air Mass Origin on Low-

Cloud Properties in the Southeast Atlantic, J. Geophys. Res. Atmos., 122(20), 11,076-11,091, doi:10.1002/2017JD027184, 2017.

Ginoux, P., Prospero, J. M., Gill, T. E., Hsu, N. C. and Zhao, M.: Global-scale attribution of anthropogenic and natural dust sources and their emission rates based on MODIS Deep Blue aerosol products, Rev. Geophys., 50(3), 1–36, doi:10.1029/2012RG000388, 2012.

Gordon, H., Field, P. R., Abel, S. J., Dalvi, M., Grosvenor, D. P., Hill, A. A., Johnson, B. T., Miltenberger, A. K., Yoshioka, M. and Carslaw, K. S.: Large simulated radiative effects of smoke in the south-east Atlantic, Atmos. Chem. Phys., 18(20), 15261–15289, doi:10.5194/acp-18-15261-2018, 2018.

Hamonou, E., Chazette, P., Balis, D., Dulac, F., Schneider, X., Galani, E., Ancellet, G. and Papayannis, A.: Characterization of the vertical structure of Saharan dust export to the Mediterranean basin, J. Geophys. Res., 104(D18), 22257, doi:10.1029/1999JD900257, 1999.

Hoffmann, L., Günther, G., Li, D., Stein, O., Wu, X., Griessbach, S., Heng, Y., Konopka, P., Müller, R., Vogel, B. and Wright, J. S.: From ERA-Interim to ERA5: considerable impact of ECMWF's next-generation reanalysis on Lagrangian transport simulations, Atmos. Chem. Phys. Discuss., 1–38, doi:10.5194/acp-2018-1199, 2018.

Holben, B. N., Eck, T. F., Slutsker, I., Tanré, D., Buis, J. P., Setzer, A., Vermote, E., Reagan, J. A., Kaufman, Y. J., Nakajima, T., Lavenu, F., Jankowiak, I. and Smirnov, A.: AERONET—A Federated Instrument Network and Data Archive for Aerosol Characterization, Remote Sens. Environ., 66(1), 1–16, doi:10.1016/S0034-4257(98)00031-5, 1998.

Holz, A., Paritsis, J., Mundo, I. A., Veblen, T. T., Kitzberger, T., Williamson, G. J., Aráoz, E., Bustos-Schindler, C., González, M. E., Grau, H. R. and Quezada, J. M.: Southern Annular Mode drives multicentury wildfire activity in southern South America., Proc. Natl. Acad. Sci. U. S. A., 114(36), 9552–9557, doi:10.1073/pnas.1705168114, 2017.

Ichoku, C., Giglio, L., Wooster, M. J. and Remer, L. A.: Global characterization of biomass-burning patterns using satellite measurements of fire radiative energy, Remote Sens. Environ., 112(6), 2950–2962, doi:10.1016/j.rse.2008.02.009, 2008.

Johansson, L., Jalkanen, J. P. and Kukkonen, J.: Global assessment of shipping emissions in 2015 on a high spatial and temporal resolution, Atmos. Environ., 167, 403–415, doi:10.1016/j.atmosenv.2017.08.042, 2017.

Jones, A. and Haywood, J. M.: Sea-spray geoengineering in the HadGEM2-ES earth-system model: radiative impact and climate response, Atmos. Chem. Phys., 12(22), 10887–10898, doi:10.5194/acp-12-10887-2012, 2012.

Jones, A., Haywood, J. and Boucher, O.: Climate impacts of geoengineering marine stratocumulus clouds, J. Geophys. Res. Atmos., 114(10), D10106, doi:10.1029/2008JD011450, 2009.

Keil, A. and Haywood, J. M.: Solar radiative forcing by biomass burning aerosol particles during SAFARI 2000: A case study based on measured aerosol and cloud properties, J. Geophys. Res. Atmos., 108(D13), n/a-n/a, doi:10.1029/2002jd002315, 2003.

Kim, M.-H. H., Omar, A. H., Tackett, J. L., Vaughan, M. A., Winker, D. M., Trepte, C. R., Hu, Y., Liu, Z., Poole, L. R., Pitts, M. C., Kar, J. and Magill, B. E.: The CALIPSO version 4 automated aerosol classification and lidar ratio selection algorithm, Atmos. Meas. Tech., 11(11), 6107–6135, doi:10.5194/amt-11-6107-2018, 2018.

Kim, S.-W., Chazette, P., Dulac, F., Sanak, J., Johnson, B. and Yoon, S.-C.: Transport and vertical structure of aerosols and water vapor over West Africa during the African monsoon dry season, Atmos. Chem. Phys. Discuss., 9(1), 1831–1871, doi:10.5194/acpd-9-1831-2009, 2009.

King, M. D., Kaufman, Y. J., Menzel, W. P. and Tanré, D.: Remote Sensing of Cloud, Aerosol, and Water Vapor Properties from the Moderate Resolution Imaging Spectrometer (MODIS), IEEE Trans. Geosci. Remote Sens., 30(1), 2–27, doi:10.1109/36.124212, 1992.

Léon, J.-F., Chazette, P., Pelon, J., Dulac, F., Randriamiarisoa, H., patrick Chazette, Pelon, J., Dulac, F. and Randriamiarisoa, H.: Aerosol direct radiative impact over the INDOEX area based on passive and active remote sensing, J. Geophys. Res., 107(D19), 8006, doi:10.1029/2000JD000116, 2002.

Lim, E.-P., Hendon, H. H., Arblaster, J. M., Delage, F., Nguyen, H., Min, S.-K. and Wheeler, M. C.: The impact of the Southern Annular Mode on future changes in Southern Hemisphere rainfall, Geophys. Res. Lett., 43(13), 7160–7167, doi:10.1002/2016GL069453, 2016.

McFarquhar, G. M. and Wang, H.: Effects of aerosols on trade wind cumuli over the Indian Ocean: Model simulations, Q. J. R. Meteorol. Soc., 132(616), 821–843, doi:10.1256/qj.04.179, 2006.

Müller, D., Ansmann, A., Mattis, I., Tesche, M., Wandinger, U., Althausen, D. and Pisani, G.: Aerosol-type-dependent lidar ratios observed with Raman lidar, J. Geophys. Res., 112(D16), D16202, doi:10.1029/2006JD008292, 2007.

Myhre, G., Samset, B. H., Schulz, M., Balkanski, Y., Bauer, S., Berntsen, T. K., Bian, H., Bellouin, N., Chin, M., Diehl, T., Easter, R. C., Feichter, J., Ghan, S. J., Hauglustaine, D., Iversen, T., Kinne, S., Kirkevåg, A., Lamarque, J.-F., Lin, G., Liu, X., Lund, M. T., Luo, G., Ma, X., van Noije, T., Penner, J. E., Rasch, P. J., Ruiz, A., Seland, Ø., Skeie, R. B., Stier, P., Takemura, T., Tsigaridis, K., Wang, P., Wang, Z., Xu, L., Yu, H., Yu, F., Yoon, J.-H., Zhang, K., Zhang, H. and Zhou, C.: Radiative forcing of the direct aerosol effect from AeroCom Phase II simulations, Atmos. Chem. Phys., 13(4), 1853–1877, doi:10.5194/acp-13-1853-2013, 2013.

794 Nicolet, M.: On the molecular scattering in the terrestrial atmosphere : An empirical formula for its calculation in
795 the homosphere, Planet. Space Sci., 32(11), 1467–1468, doi:10.1016/0032-0633(84)90089-8, 1984.
796 Oreopoulos, L. and Platnick, S.: Radiative susceptibility of cloudy atmospheres to droplet number perturbations:
797 2. Global analysis from MODIS, J. Geophys. Res., 113(D14), D14S21, doi:10.1029/2007JD009655, 2008.
798 Parmar, R. S., Welling, M., Andreae, M. O. and Helas, G.: Water vapor release from biomass combustion, Atmos.
799 Chem. Phys., 8(20), 6147–6153, doi:10.5194/acp-8-6147-2008, 2008.
800 Ramanathan, V., Li, F., Ramana, M. V, Praveen, P. S., Kim, D., Corrigan, C. E., Nguyen, H., Stone, E. A., Schauer,
801 J. J., Carmichael, G. R., Adhikary, B. and Yoon, S. C.: Atmospheric brown clouds: Hemispherical and regional
802 variations in long-range transport, absorption, and radiative forcing, J. Geophys. Res, 112, 22–21,
803 doi:10.1029/2006JD008124, 2007.
804 Raut, J.-C. and Chazette, P.: Radiative budget in the presence of multi-layered aerosol structures in the framework
805 of AMMA SOP-0, Atmos. Chem. Phys., 8(4), 12461–12528, doi:10.5194/acpd-8-12461-2008, 2008.
806 Raut, J.-C. and Chazette, P.: Assessment of vertically-resolved PM_{10} from mobile lidar observations,
807 Atmos. Chem. Phys., 9(21), 2009.
808 Remer, L. A., Kaufman, Y. J., Tanré, D., Mattoo, S., Chu, D. A., Martins, J. V., Li, R.-R., Ichoku, C., Levy, R. C.,
809 Kleidman, R. G., Eck, T. F., Vermote, E. and Holben, B. N.: The MODIS Aerosol Algorithm, Products, and
810 Validation, J. Atmos. Sci., 62(4), 947–973, doi:10.1175/JAS3385.1, 2005.
811 Royer, P., Raut, J.-C., Ajello, G., Berthier, S. and Chazette, P.: Synergy between CALIOP and MODIS instruments
812 for aerosol monitoring: application to the Po Valley, Atmos. Meas. Tech., 3(4), 893–907, doi:10.5194/amt-3-893-
813 2010, 2010.
814 Royer, P., Chazette, P., Lardier, M. and Sauvage, L.: Aerosol content survey by mini N_2-Raman lidar:
815 Application to local and long-range transport aerosols, Atmos. Environ., 45(39),
816 doi:10.1016/j.atmosenv.2010.11.001, 2011a.
817 Royer, P., Chazette, P., Lardier, M. and Sauvage, L.: Aerosol content survey by mini N2-Raman lidar: Application
818 to local and long-range transport aerosols, Atmos. Environ., 45(39), 7487–7495,
819 doi:10.1016/j.atmosenv.2010.11.001, 2011b.
820 Royer, P., Chazette, P., Sartelet, K., Zhang, Q. J., Beekmann, M. and Raut, J.-C.: Comparison of lidar-derived
821 PM_{10} with regional modeling and ground-based observations in the frame of MEGAPOLI experiment, Atmos.
822 Chem. Phys., 11(20), 10705–10726, doi:10.5194/acp-11-10705-2011, 2011c.
823 Salmonson, V. V., Barnes, W. L. L., Maymon, P. W. P. W. P. W., Montgomery, H. E. H. E. and Ostrow, H.:
824 MODIS: Advanced Facility Instrument for Studies of the Earth as a System, IEEE Trans. Geosci. Remote Sens.,
825 27(2), 145–153, doi:10.1109/36.20292, 1989.
826 Stein, A. F., Draxler, R. R., Rolph, G. D., Stunder, B. J. B., Cohen, M. D., Ngan, F., Stein, A. F., Draxler, R. R.,
827 Rolph, G. D., Stunder, B. J. B., Cohen, M. D. and Ngan, F.: NOAA's HYSPLIT Atmospheric Transport and
828 Dispersion Modeling System, Bull. Am. Meteorol. Soc., 96(12), 2059–2077, doi:10.1175/BAMS-D-14-00110.1,
829 2015.
830 Stier, P., Schutgens, N. A. J., Bellouin, N., Bian, H., Boucher, O., Chin, M., Ghan, S., Huneeus, N., Kinne, S., Lin,
831 G., Ma, X., Myhre, G., Penner, J. E., Randles, C. A., Samset, B., Schulz, M., Takemura, T., Yu, F., Yu, H. and
832 Zhou, C.: Host model uncertainties in aerosol radiative forcing estimates: results from the AeroCom Prescribed
833 intercomparison study, Atmos. Chem. Phys., 13(6), 3245–3270, doi:10.5194/acp-13-3245-2013, 2013.
834 Stohl, A.: Computation, accuracy and applications of trajectories - A review and bibliography, Atmos. Environ.,
835 32(6), 947–966, doi:10.1016/S1352-2310(97)00457-3, 1998.
836 Swap, R. J., Annegarn, H. J., Suttles, J. T., King, M. D., Platnick, S., Privette, J. L. and Scholes, R. J.: Africa
837 burning: A thematic analysis of the Southern African Regional Science Initiative (SAFARI 2000), J. Geophys.
838 Res. Atmos., 108(D13), n/a-n/a, doi:10.1029/2003JD003747, 2003.
839 Trenberth, K. E.: Interannual Variability of the 500 mb Zonal Mean Flow in the Southern Hemisphere, Mon.
840 Weather Rev., 107(11), 1515–1524, doi:10.1175/1520-0493(1979)107<1515:ivotmz>2.0.co;2, 2002.
841 Tyson, P. D. and Preston-White, R. A.: The weather and climate of southern Africa, Oxford University Press.
842 [online] Available from: https://global.oup.com/academic/product/the-weather-and-climate-of-southern-africa-
843 9780195718065?lang=en&cc=in (Accessed 29 April 2019), 2000.
844 Vickery, K. J., Eckardt, F. D. and Bryant, R. G.: A sub-basin scale dust plume source frequency inventory for
845 southern Africa, 2005-2008, Geophys. Res. Lett., 40(19), 5274–5279, doi:10.1002/grl.50968, 2013.
846 Winker, D. M., Hunt, W. H. and McGill, M. J.: Initial performance assessment of CALIOP, Geophys. Res. Lett.,
847 34(19), L19803, doi:10.1029/2007GL030135, 2007.
848 Yorks, J. E., McGill, M. J., Palm, S. P., Hlavka, D. L., Selmer, P. A., Nowottnick, E. P., Vaughan, M. A., Rodier,
849 S. D. and Hart, W. D.: An overview of the CATS level 1 processing algorithms and data products, Geophys. Res.
850 Lett., 43(9), 4632–4639, doi:10.1002/2016GL068006, 2016.
851 Zuidema, P., Sedlacek, A. J., Flynn, C., Springston, S., Delgadillo, R., Zhang, J., Aiken, A. C., Koontz, A. and
852 Muradyan, P.: The Ascension Island Boundary Layer in the Remote Southeast Atlantic is Often Smoky, Geophys.
853 Res. Lett., 45(9), 4456–4465, doi:10.1002/2017GL076926, 2018.

854

Appendix A: Ground-based lidar analysis – link with spaceborne lidar observations

856 **A.1   Description of the ground-based lidar**

857 The ground-based lidar system used at the Henties Bay site is the ALS450® lidar manufactured by Leosphere and
858 initially developed by the Commissariat à l'Energie Atomique (CEA) and the Centre National de la Recherche
859 Scientifique (CNRS) (Royer et al., 2011a). The lidar emission is based on an Ultra® Nd:YAG laser manufactured
860 by Quantel, delivering 6 ns width pulses at the repetition rate of 20 Hz with a mean pulse energy of 16 mJ at a
861 wavelength of 355 nm. This system is particularly well-adapted to measure tropospheric aerosol profiles in the
862 lower and middle troposphere. Its high vertical resolution of ~15 m after filtering and temporal resolution (~1
863 minute) gives the advantage of being able to follow the fast vertical evolutions of the atmospheric scattering layers
864 and to accurately locate the aerosol layers within the troposphere. The lidar is composed of two receiver channels
865 dedicated to the measurement of the co-polar and cross-polar signals. The detection is carried out by
866 photomultiplier tubes and narrowband filters with a bandwidth of 0.5 nm. Its main characteristics are summarized
867 in Table A1 where we have added the features of the LNG lidar for comparison.

868

869 **Table A1**: **Main characteristics of both the ALS and LNG lidars.**

	Ground-based lidar ALS	Airborne lidar LNG
Laser	Nd:YAG, flash-pumped, Q-switched Q-smart QUANTEL	Flashlamp-pumped Nd:YAG Q-switched oscillator (Quantel YG980)
Pulse duration	6 ns	6 ns @ 335 nm 7 ns @ 532 nm 8 ns @ 1064 nm
Reception channels	// 354.7 nm ⊥ 354.7 nm	// 355, 532 and 1064 nm ⊥ 355 nm
Emitted energy	16 mJ	50 mJ @ 335 nm 10 mJ @ 532 nm 50 mJ @ 1064 nm
Frequency	20 Hz	20 Hz
Reception diameter	15 cm	30 cm (Cassegrain telescope)
Field-of-view	~2.3 mrad	0.5 mrd @ 335 nm 6 mrd @ 532 nm 8 mrd @ 1064 nm
Filter bandwidth/transmission	0.5 nm / 70% @ 335 nm // and ⊥	5 nm/ 25% @ 335 nm // and ⊥ 0.2 nm / 25% @ 532 nm 1 nm / 30% @ 1064 nm
Detector	Photomultiplier (PM) tubes	PM Hamamatsu H6780-04 @ 355 nm

		PM Hamamatsu H6780-02 @ 532 nm APD Perkin-Elmer C30659-1060 @ 1064 nm
Post-processing vertical resolution	15-30 m	6 m
Post-processing Temporal resolution	Variable, see Table 1	1 minute

870

A.2   Overlap correction and rightness of lidar profiles

In order to derive aerosol extinction coefficient profiles (AEC), the lidar apparent backscatter coefficient (ABC) in the aerosol-free portions of the vertical profiles must be assessed and must follow the slope of the molecular backscattering. The ABC, also called the total attenuated backscatter coefficient (Royer et al., 2011a), correspond to the raw lidar signal corrected for both the contribution of the sky background and the solid angle, as in the Equation (3) of Royer et al. (2010).

Furthermore, close to the lidar emission source the overlap factor generated by the overlap defects of the laser emission and telescope reception fields also needs to be assessed. The overlap factor is derived from measurements acquired in the horizontal line of sight, with the hypothesis of a homogeneous atmosphere along the line of sight between the emission and a distance of 1.5 km. The overlap factor and the associated standard deviation are shown in Figure A1. It can be considered that the correction of the overlap factor induces a relative error lower than 15% for an overlap factor between 0.8 and 1 (Chazette, 2003), corresponding to a distance of 150 m from the emitter. The molecular contribution is obtained from the Era5 pressure and temperature data at the horizontal resolution of 0.25° using the Nicolet model (Nicolet, 1984). The error on the aerosol extinction coefficient due to uncertainty on the molecular density remains below 2-3% (Chazette et al., 2012b). The main sources of uncertainty are the shoot noise and the atmospheric variability during the measurement. Both are taken into account for each retrieved profile.

A representative time-average lidar profiles of the ABC over the duration of the measurement field campaign is shown in Figure A2. The dates were chosen to be representative of the dataset of lidar vertical profiles encountered during the AEROCLO-sA campaign. The curves in black are the ABC profiles and those in red correspond to the molecular backscatter coefficient computed using ERA5 data. We note that in the top of the profiles there is a very good agreement that ensures that the lidar is well aligned. The area comprised between the black and red curves corresponds to the contribution of atmospheric aerosols and, in the upper part of the profiles, to that of optically thin clouds (Figure A2c and d). The aerosol content increases rapidly between 22 and 28 August, showing a significant evolution of aerosol contributions in the free troposphere (FT), between 1 and 5 km above the mean sea level (AMSL). It is notable that the vertical profiles of the ABC vary little during the averaging period, the average profiles are therefore quite representative of the state of the atmosphere for all the considered periods.

898
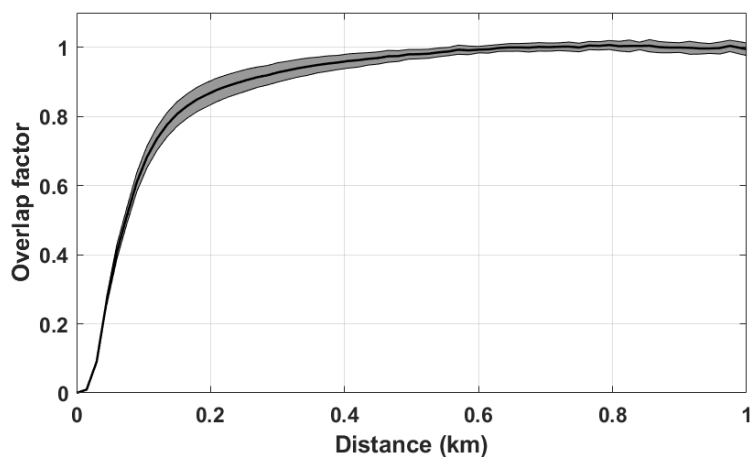
Figure A1: Overlap factor of the ALS (continuous black line) and its standard deviation (grey area).

900

A.3 Ground-based lidar data processing using external constraints

The inversion procedure to retrieve the aerosol optical properties from ALS is well documented in previous articles where uncertainty sources are exhaustively quantified (e.g. Raut and Chazette, 2009; Royer et al., 2011b; Chazette et al., 2012a). In the present case, where a simple elastic backscattering lidar is used, we use additional constraints to the lidar equation using sun photometer-derived aerosol optical thickness (AOT) when available, but also the aerosol typing determined from the CALIOP and CATS measurements for cases where the orbit allowed the sampling of aerosols present in the FT. Figure A3 gives the example of the case of the geographical coincidence between the night CALIOP (CATS) orbit on 28 (30) August 2017 and the lidar measurements above the Henties Bay site. All available CALIOP and CATS orbits passing over Namibia were analysed and the results in terms of aerosol typing are given in Table 1 and Table 2. The correspondences in terms of LR are given in Table 2 for both instruments.

In the area of interest, aerosol properties are different in the planetary boundary layer (PBL), where the composition is dominated by marine and coastal dust emissions, and in the FT where the composition is dominated by long-range transport of BBA and dust emitted over the continental plateau. Therefore, we have used different values of LR in the PBL and in the FT to perform the lidar inversion when lidar measurements were acquired concomitantly with sun photometer AOT measurements. The LR in the FT is derived from the aerosol typing performed by the space-borne lidars (see Table 2). When there is no CALIOP or CATS overpasses we take the value of LR of the nearest day also considering the shape of the AEC profile and the origin of air masses using back trajectories. Values of 65-70±25 sr and 55±25 sr at 532 nm are used for the two main aerosol types sampled, namely smoke and polluted dust, respectively. The ground-based lidar in Henties Bay operates at 355 nm, the LR value is then different. Müller et al. (2007) showed that LR values at 355 and 532 nm differ by about of 20% for forest fire smoke and less than 10% for dust aerosols (see the Table 1 of their paper), widely included in the expected uncertainty in LRs for spaceborne lidar. In the PBL, the LR values are selected from the discrete set of lidar ratios shown in Table 2 via a minimization of the difference of AOT between the ground-based lidar and the sun photometer: the LR in the PBL is adjusted so that the AOT calculated from the lidar AEC profile matches best the AOT from the sun photometer at 355 nm. The LR values obtained during the field campaign are associated with clean marine air aerosols (i.e. 20-23 sr) and polluted dust (i.e. 55 sr). This was done for all days listed in Table 3, with the exception of 8 and 9 September 2017. On those days, the sun photometer AOT could not be used to constrain the inversion of the lidar measurements. This is likely due to the presence of unscreened clouds in the sun photometer inversion (as logged by the ground-based lidar on 8 September, Figure A2d). For those two days, we have used a LR of 20 sr in the PBL to be able to invert the lidar data. Note that the use of a value of 55 sr in the PBL on those days (i.e. the value retrieved for the previous days) leads to an unrealistically high lidar-derived AOT. As a consequence, we observed an underestimation of the lidar-derived AOT when compared to the sun photometer level 2 product.

Besides the determination of the AEC, we also evaluated the linear particle depolarization ratio (PDR) values using an approach described in Chazette et al. (2012b). A detailed study of uncertainties for different aerosol types can

942 be found in Dieudonné et al. (2017). Statistical errors of 2% on the PDR can be expected due to statistical noise
943 but the biais linked to the uncertainty on the LR increases these errors.
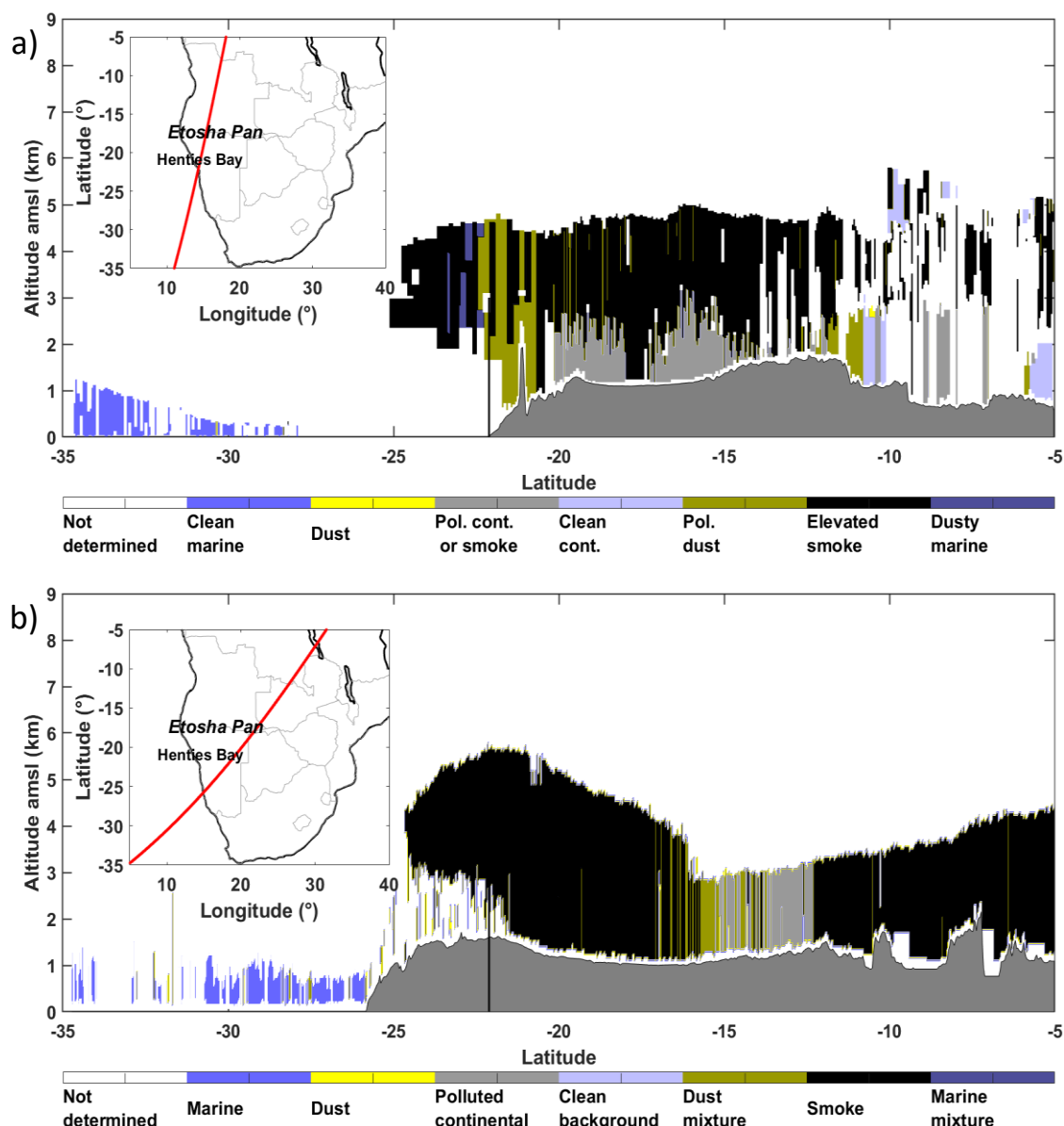
944
945 Figure A4 presents two vertical profiles on 22 August and 7 September 2017 which have been considered to
946 illustrate the error due to the choice of the LR. The AEC is affected by less than 0.02 km^{-1} except at the upper part
947 of the profile on 7 September when the attenuation strongly decreases the signal to noise ratio. The AOTs at 355
948 nm are 0.36 on 22 August and 1.31 on 7 September. Accounting for the uncertainty on the LR of ±25 sr, the AOTs
949 range from 0.34 to 0.39 and from 1.25 to 1.37 on 22 August and 7 September, respectively. The PDR can be more
950 affected than the AEC, mainly when the AEC is smaller (< 0.1 km^{-1}). Nevertheless, in the aeorsol layers, the
951 uncertainties due to the LR is smaller than 2-3%. All these uncertainty sources do not significantly impact the
952 scientific findings.

953

954 **Figure A3: a) CALIOP-derived aerosol typing for the night time orbit (10.2017-08-28T00-08-17ZN) on 28 August 2017.**
955 **b) CATS-derived aerosol typing for the night time orbit (2017-08-30T00-32-37T01-18-13UT) on 30 August 2017. The**

956 latitudinal location of the Henties Bay site is given by the vertical black line. Inserted panels in a) and b) show the
957 position of the space-borne lidar tracks over southern Africa and with respect to Henties Bay.
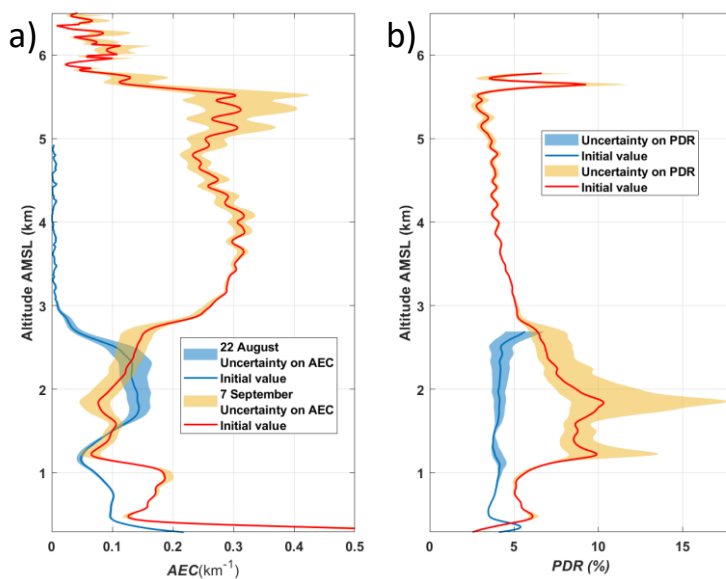
958

959 Figure A4: Vertical profiles of the aerosol extinction coefficient (AEC) and particle depolarization ratio (PDR) at 355
960 nm: on a) 22 August 2017 and b) 7 September 2017. The shaded areas give the uncertainty linked to the one on the lidar
961 ratio (LR) of ±25 sr as considered for the CALIOP operational algorithm.